

Constraining the mass of a fermionic dark matter particle via phase space bounds in dwarf spheroidal galaxies

THESIS

submitted in partial fulfillment of the requirements for the degree of

MASTER OF SCIENCE in PHYSICS

Author :Victoria Tarisai TikiStudent ID :s2144530Supervisor :Dr Alexey Boyarsky2nd corrector :Dr Vadim Cheianov

Leiden, The Netherlands, July 14, 2020

Constraining the mass of a fermionic dark matter particle via phase space bounds in dwarf spheroidal galaxies

Victoria Tarisai Tiki

Instituut-Lorentz for Theoretical Physics, Leiden University Niels Bohrweg 2, Leiden, 2333 CA, The Netherlands

July 14, 2020

Abstract

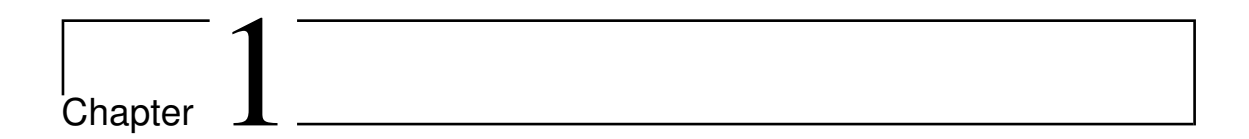
The *Tremaine-Gunn* bound may be used to estimate the minimum mass required for a fermionic dark matter particle to obey the limiting condition $F \leq \frac{g}{(2\pi\hbar)^3}$ for phase space density F. In principle, knowledge of the matter density profile of a dark matter dominated galaxy is enough to reconstruct a coarse grained phase space density (also subject to this limit) using an estimate for the maximal velocity (e.g. the escape velocity or velocity dispersion). Here, several works proposing density profiles are explored. We can show that one of these theories, the *Ruffini-Argüelles-Rueda* model, suffers from significant inconsistencies. Finally, we discuss the *Richardson-Fairbairn* profiles, which result from an extended Jeans analysis, i.e. a fitting procedure based on Jeans and Virial equations. We apply the largely model-robust Tremaine-Gunn bound to data generated by *Read et Steger* (using a variant of the Richardson-Fairbairn model) for Local Group dwarf spheroidal galaxies and obtain a lower mass bound for a fermionic dark matter particle: $m \geq 180^{+51}_{-43}eV$

Contents

1	Intr	roduction	7
	1.1	Tremaine-Gunn bound	8
	1.2	Jeans equations	11
		1.2.1 Boltzmann equation	12
		1.2.2 Velocity distribution	12
		1.2.3 Jeans equations	15
		1.2.4 Virial equations	18
2	Dar	rk Matter Density Models	21
	2.1	Randall-Scholtz-Unwin Model	21
		2.1.1 Model	21
		2.1.2 Limitations	24
	2.2	Ruffini-Argüelles-Rueda Model	25
		2.2.1 Model	25
		2.2.2 Limitations	30
	2.3	Brownsberger-Randall Model	33
		2.3.1 Model	34
		2.3.2 Validity	38
3	Low	ver mass bound with parametrized dark matter	models 41
	3.1	Richardson-Fairbairn profiles	41
		3.1.1 Comparison to Read-Steger profiles	46
	3.2	Mass bounds	49
		3.2.1 Profiles	49
		3.2.2 Bounds	51
		3.2.3 Corrections	53
4	Ack	knowledgements	59
5	Bib	liography	61

-			11	`		r	7	EN	TF	T-/	$\overline{}$
٦	1	(()		1	Н	1	NI.	ľ	٦
J		•	~	╱.	LV		_		N	1	_

A	Deriving Jeans and Virial equations A.1 Deriving the 2nd order Jeans equation	65 65
	A.2 Deriving the Virial equation	66
В	Density profiles	69
	B.1 Density profile comparison	69
C	Mass Bounds	71



Observations of galactic dynamics suggest that the universe's matter content is dominated by a type of non-luminous matter. This type of matter is baptised dark matter, with properties yet to be specified. Evidence for this theory comes from a multitude of sources. Famously, the gravitational force exerted by luminous matter in the Milky Way cannot account for the rotational velocities of stars in the sun's interstellar neighbourhood. From measuring velocity dispersions in galactic clusters, one can further conclude (due to research by *F. Zwicky* [1]) that luminous matter alone is not sufficient to keep these galaxies bound. [2] Other observations hinting at the existence of dark matter are the small-scale structure of the Cosmic Microwave Background, the large-scale structures of galaxies we observe today, data from galactic collisions such as the Bullet Cluster, and gravitational lensing. [3]



Figure 1.1: Photograph of the Sextans dwarf spheroidal from [4]

The total dark matter content makes up 27% of the universe's total mass-

energy content, with luminous matter only contributing with 5%. Dark matter cannot be observed directly, as it doesn't partake in electromagnetic interaction. However, it can be probed via its gravitational interaction with visible matter. [5] A Dwarf Spheroidal Galaxy (dSph) is an appropriate point of departure when looking for dark matter, as these types of galaxies are not very luminous and thought to be dominated by dark matter. [6] The dSphs orbiting the Milky Way Galaxy are listed in table 1.1. One of those Local Group (LG) dSphs is the Sextans dwarf spheroidal, as shown in figure 1.1.

1.1 Tremaine-Gunn bound

The Tremaine-Gunn bound, after American physicists Scott Tremaine and James E. Gunn, is commonly used to derive an estimate for the minimum mass of a fermionic dark matter particle based on galactic phase space density considerations. For fermionic dark matter, this lower bound is model robust. However, when applied to real models some assumptions which impact its accuracy are typically made. These limitations will be discussed in the following, alongside the general derivation and applications of the bound.

The phase-space density F generally describes the number density of particles within a phase-space volume d^3qd^3p centred around phase-space coordinates (\mathbf{q},\mathbf{p}) . The Tremaine-Gunn bound, as found in [7], assumes fermionic dark matter particles with a phase space density F_{DM} that can not exceed that of the most densely packed, i.e. fully degenerate, Fermi gas:

$$F_{DM} \le F_{max} = \frac{g}{(2\pi\hbar)^3} \tag{1.1}$$

with *g* as the degrees of freedom of the dark matter particle in question. This maximum can be inferred from the maximum value for a general Fermi-Dirac distribution. *

$$F_{FD}(q,p) = \frac{g}{(2\pi\hbar)^3} \frac{1}{e^{\frac{E(p)-\mu(q)}{k_BT(q)}} + 1}$$
(1.2)

If an expression for the phase space density as a function of the dark matter particle mass m_{DM} is known, then inequality (1.1) can be solved to give a limit for this mass m_{DM} . The dark matter phase space density F_{DM} is difficult to access in practice. One possible estimate, as <u>performed</u> by *Boyarsky et alii* [8], introduces a coarse-grained phase space density F_{DM} . The coarse grained phase space density,

^{*}In addition to the value for F_{max} given above, *Boyarsky et alii* [8] introduce a slightly alternative measure: The Liouville theorem implies that the maximum of the phase-space density does not change in time. For a relativistic primordial Fermi-Dirac distribution, F_{max} then becomes $\frac{g}{2(2\pi\hbar)^3}$, which, for $E(p)\gg\mu$, can be inferred from equation 1.2. The resulting lower mass bound becomes more strict by a factor of $2^{1/4}$. However, this bound makes assumptions about the evolution of the phase-space density.

obtained by averaging over phase space cells (see equation 1.3), may not exceed the value for the fine-grained phase-space density F_{DM} . This implies $\overline{F_{DM}} \leq F_{DM} \leq F_{max}$, with

$$\overline{F_{DM}}(p,q) = \frac{1}{vol(\Delta\Pi)} \int_{\Delta\Pi(p,q)} d\Pi' F_{DM}(p',q')$$
(1.3)

where averaging goes over the collective of phase space cells $\Delta\Pi(q,p)$, centred around the phase space coordinates (q,p). The maximally coarse-grained phase-space density, a result of averaging over a phase space volume such that the entire spherically symmetric galaxy's dark matter content is contained within, reads

$$\overline{F_{DM}} = \frac{M}{m_{DM} V_{rs} V_{ms}} = \frac{M}{(\frac{4}{3}\pi)^2 R^3 m_{DM}^3 v_{esc}^3}$$
(1.4)

M denotes the galaxy's total mass, V_{rs} the volume in real space, ad V_{ms} the volume in momentum space. The galaxy's entire phase space volume is approximated by $vol(\Delta\Pi) = V_{rs}V_{ms} = (\frac{4}{3}\pi)^2R^3m_{DM}^3v_{esc}^3$. The maximum velocity of a dark matter particle was taken to be the escape velocity. Typically, M and v_{esc} are inferred from observation. Together with equation (1.1), this can be solved to yield:

$$m_{DM}^4 \ge \frac{9M\pi\hbar^3}{2gR^3v_{esc}^3} = \frac{9\pi\hbar^3}{2^{5/2}gG^{3/2}R^{3/2}M^{1/2}}$$
(1.5)

where, following *Boyarsky et alii* [8], in the last equality, $v_{esc} = \sqrt{\frac{2GM}{R}}$ was used. Together with maximal-coarse graining, this assumes that the phase space density is evaluated at the outer edge of the spherical galaxy (i.e. $R = r_{edge}$), after which the density drops to zero. If equation (1.5) is applied to any other point r within the dark matter halo, then two issues arise:

- the escape velocity (if taken as $v_{esc}=\sqrt{\frac{2GM(r)}{r}}$) will be underestimated and, therefore, the lower mass bound m_{DM} overestimated
- due to the ellipticity of the orbits, dark matter particles found at radius r may occupy a volume V_{rs} that extends past r. This means that the maximally coarse-grained phase space volume is underestimated and, therefore, the lower mass bound overestimated

Besides this overestimation, this method also assumes the galaxy to be spherically symmetric. Instead, true sphericities for LG dSphs range between 0.5 to 0.9, according to *Łokas et alii* [9]

These considerations aside, a convenient choice for the radius *r* at which equation

(1.5) is to be evaluated is the 3D half-light radius r_{12} . It is the radius describing the spherical surface that encloses half of the galaxy's luminosity and, somewhat astoundingly, resolves enclosed masses $M(r_{12})$ with comparatively low deviations across different dark matter models [10] † . This apparent model independence of the measured value of $M(r_{12})$ makes r_{12} a viable point to evaluate equation (1.5) at, although overestimation may still be an issue in this case.

A physically equivalent restriction to equations (1.1) and (1.4) is to impose that the Fermi velocity v_{deg} (corresponding to a fully degenerate system) may not exceed the escape velocity of the system [8]:

$$v_{deg} = \hbar \left(\frac{6\pi^2 M}{gm_{DM}^4 V} \right)^{\frac{1}{3}} \le v_{max}(r) = v_{esc}(r)$$
 (1.6)

Presuming that the bound is evaluated at the edge of the galaxy ($v_{esc}(r) = \sqrt{\frac{2GM}{r}}$), this formula yields the same bound as the one based on the maximally coarse-grained phase space density (equation (1.4)). Besides the coarse-grained measure in equation (1.5), we will, in the following chapters, also consider another, albeit not maximally, coarse-grained measure for the phase-space density. This measure results from looking at a single phase space cell and integrating over all of momentum space at a given point r (rather than integrating over all of spatial and momentum space as done for the maximally coarse grained measure):

$$\overline{F_{DM}}(r) = \frac{1}{vol(\Delta p)} \int_{\Delta p} dp' F_{DM}(p', r)$$
 (1.7)

With $vol(\Delta p) = V_{ms} = \frac{4}{3}\pi p_{max}^3$, the new coarse-grained measure then reads

$$\overline{F_{DM}}(r) = \frac{\rho(r)}{m_{DM}V(r)_{ms}} = \frac{\rho(r)}{m_{DM}^4 \frac{4}{3}\pi v_{esc}^3(r)}$$
(1.8)

which, together with equation (1.1), leads to the mass bound

$$m_{DM} \ge \left(\frac{\hbar^3 6\pi^2 \rho(r)}{g v_{esc}^3(r)}\right)^{1/4} \tag{1.9}$$

Alternatively to the escape velocity v_{esc} , one may also choose the velocity dispersion $\sigma^2(r)$ as an estimate for the maximum velocity (see e.g. [8]). The

[†]In contrast to the 3D half-light radius, the 2D projected half light-radius R_e may also be defined. For a projection of the galaxy under consideration onto the sky, R_e is the radius describing the *circle* enclosing half of the projected galaxy's luminosity as viewed *in the plane of the sky*. This radius is smaller than the 3D half-light radius r_{12} , but does not possess the property of minimizing the uncertainty in the mass profile

1.2 Jeans equations 11

velocity dispersion is a moment of the generally unknown velocity probability density function and, although highly model-dependent, may be inferred from data. Assuming some probability density function (e.g. Normal distribution), the maximum velocity can be approximated based on the velocity dispersion. This method has the advantage of generally yielding lower values for the maximum velocity than the escape velocity and can, therefore, lead to a higher, i.e. more consequential, lower mass bound.

	m [keV]
Carina	$0.215_{0.032}^{0.050}$
Draco	$0.226_{0.016}^{0.020}$
Fornax	$0.164_{0.026}^{0.041}$
LeoI	$0.189_{0.034}^{0.059}$
LeoII	$0.269_{0.035}^{0.052}$
Sculptor	$0.264_{0.031}^{0.038}$
Sextans	$0.147^{0.044}_{0.026}$
UMi	$0.195^{0.051}_{0.031}$

Table 1.1: lower mass bounds from LG dSphs as found in [8]. Note that these mass bounds were evaluated at the 2D projected half light radius R_e (i.e. equation (1.5) with $r = R_e$ and $M = M(R_e)$) for the maximally coarse-grained phase-space density. If one assumes that $F_{max} = \frac{g}{2(2\pi\hbar)^3}$ (see footnote), all the given bounds are higher by a factor $2^{1/4}$.

Applied to the Local Group dwarf spheroidal galaxies, the Tremaine-Gunn bound gives lower masses in the 100 eV range (see table 1.1).

1.2 Jeans equations

In order to apply the Tremaine-Gunn bound to LG dSPhs, one needs to derive an expression for the dark matter phase space density $F_{DM}(r)$. Using approximations to the phase space density such as equation 1.4, it is necessary to derive an enclosed mass profile M(r) (or mass density profile $\rho(r)$) and an expression for the maximum velocity v_{max} . As stated in the previous chapter, escape velocities (as a function of mass profile) or velocity dispersions may be used as a measure for v_{max} . Jeans equations describe the motions of either dark matter particles or luminous matter in galaxies by relating densities, gravitational potentials and moments of the velocity probability density with one another. This makes Jeans analysis a convenient first approach for deriving dark matter density models. The following derivation of Boltzmann equation, moments of the velocity distribution and Jeans equations closely follows *Binney et Tremaine* [11].

1.2.1 Boltzmann equation

For their derivation, *Binney et Tremaine* treat the stars (or dark matter particles) as identical collisionless point masses that are continuously distributed in space, which is valid for a system with many thousands of stars. They define the distribution function $f(\mathbf{q}, \mathbf{p})$ as a function describing the probability that any given star in the galaxy will be found in the phase space volume d^3qd^3p , centred around the generalized position \mathbf{q} and generalized momentum \mathbf{p} . This distribution function, i.e. the probability per unit phase space volume, is related to the phase space density $F_{DM}(q, p)$ via $F_{DM}(q, p) = Nf(q, p)$, where N is the number of stars/particles in the galaxy. Naturally, this distribution function is normalized to give

$$\int_{galaxy} f(\mathbf{q}, \mathbf{p}) d^3q d^3p = 1 \tag{1.10}$$

The collisionless Boltzmann equation is a direct consequence of the conservation of probability:

$$\frac{\partial f}{\partial t} + \frac{\partial}{\partial \mathbf{q}}(f\dot{\mathbf{q}}) + \frac{\partial}{\partial \mathbf{p}}(f\dot{\mathbf{p}}) = 0 \tag{1.11}$$

With $f = f(\mathbf{q}, \mathbf{p})$. Using Hamilton's equation $(\frac{\partial H}{\partial q} = -\dot{p}; \frac{\partial H}{\partial p} = \dot{q})$ this can be rewritten to yield the collisionless Boltzmann equation:

$$\frac{\partial f}{\partial t} + \dot{\mathbf{q}} \frac{\partial f}{\partial \mathbf{q}} + \dot{\mathbf{p}} \frac{\partial f}{\partial \mathbf{p}} = 0 \tag{1.12}$$

In Cartesian coordinates the Hamiltonian reads $H=\frac{1}{2}(p_x^2+p_y^2+p_z^2)+\Phi(x,y,z)$ and the collisionless Boltzmann equation thus becomes

$$\frac{\partial f}{\partial t} + \mathbf{p} \frac{\partial f}{\partial \mathbf{x}} - \frac{\partial \Phi}{\partial \mathbf{x}} \frac{\partial f}{\partial \mathbf{p}} = 0 \tag{1.13}$$

In a spherical coordinate system, the Hamiltonian takes on the form: $H = \frac{1}{2}(p_r^2 + \frac{p_\theta^2}{r^2} + \frac{p_\phi^2}{r^2\sin^2\theta}) + \Phi(r,\theta,\phi)$, which lets us recast equation (1.12) as

$$\frac{\partial f}{\partial t} + p_r \frac{\partial f}{\partial r} + \frac{p_\theta}{r^2} \frac{\partial f}{\partial \theta} + \frac{p_\phi}{r^2 \sin^2 \theta} \frac{\partial f}{\partial \phi} - \left(\frac{\partial \Phi}{\partial r} - \frac{p_\theta^2}{r^3} - \frac{p_\phi^2}{r^3 \sin^2 \theta}\right) \frac{\partial f}{\partial p_r} - \left(\frac{\partial \Phi}{\partial \theta} - \frac{p_\phi^2 \cos \theta}{r^2 \sin^3 \theta}\right) \frac{\partial f}{\partial p_\theta} - \frac{\partial \Phi}{\partial \phi} \frac{\partial f}{\partial p_\phi} = 0$$
(1.14)

1.2.2 Velocity distribution

Generally speaking, Jeans equations are obtained by integrating the collisionless Boltzmann equations over momentum space. In order to rewrite the resulting 1.2 Jeans equations 13

equations, it is convenient to utilize expressions for the moments of the velocity distribution function $P_{\mathbf{x}}(\mathbf{v})$. The velocity distribution function gives the probability for a chosen star with position \mathbf{x} to be found with velocity \mathbf{v} . Using the usual relations for conditional probability, $P_{\mathbf{x}}(\mathbf{v})$ can easily be expressed as:

$$P_{\mathbf{x}}(\mathbf{v}) = \frac{f(\mathbf{x}, \mathbf{v})}{\nu(\mathbf{x})}$$
(1.15)

where $\nu(\mathbf{x})$ is the probability to find the given star at position \mathbf{x} regardless of its velocity. An expression for $\nu(\mathbf{x})$ is achieved by integrating out the dependence of $f(\mathbf{x}, \mathbf{v})$ on the velocity.

$$\nu(\mathbf{x}) = \int f(\mathbf{x}, \mathbf{v}) d^3 v \tag{1.16}$$

Other distribution functions, such as $P_{\mathbf{x}}(v_x)$, the probability of finding the star with velocity v_x in x-direction, similarly, can be obtained by integrating out dependence on velocities in other directions. This makes writing down the moments of the velocity distribution a simple task.

In Cartesian coordinates:

$$\overline{v_x}(\mathbf{x}) = \frac{1}{\nu(\mathbf{x})} \int v_x f(\mathbf{x}, \mathbf{v}) dv_x dv_y dv_z$$

$$\overline{v_y}(\mathbf{x}) = \frac{1}{\nu(\mathbf{x})} \int v_y f(\mathbf{x}, \mathbf{v}) dv_x dv_y dv_z$$

$$\overline{v_z}(\mathbf{x}) = \frac{1}{\nu(\mathbf{x})} \int v_z f(\mathbf{x}, \mathbf{v}) dv_x dv_y dv_z$$
(1.17)

In spherical coordinates, the canonical momenta read

$$p_r = \dot{r} = v_r$$
 $p_\theta = r^2 \dot{\theta} = r v_\theta$ $p_\phi = r^2 \sin^2 \theta \dot{\phi} = r \sin \theta v_\phi$ (1.18)

and, thus, the moments become

$$\overline{p_r}(\mathbf{x}) = \frac{1}{\nu(\mathbf{x})} \int p_r f(\mathbf{x}, \mathbf{v}) dv_r dv_\theta dv_\phi \to \int f p_r d^3 p = r^2 \sin \theta \nu(\mathbf{x}) \overline{p_r}(\mathbf{x})
\overline{p_\theta}(\mathbf{x}) = \frac{1}{\nu(\mathbf{x})} \int p_\theta f(\mathbf{x}, \mathbf{v}) dv_r dv_\theta dv_\phi \to \int f p_\theta d^3 p = r^2 \sin \theta \nu(\mathbf{x}) \overline{p_\theta}(\mathbf{x})
\overline{p_\phi}(\mathbf{x}) = \frac{1}{\nu(\mathbf{x})} \int p_\phi f(\mathbf{x}, \mathbf{v}) dv_r dv_\theta dv_\phi \to \int f p_\phi d^3 p = r^2 \sin \theta \nu(\mathbf{x}) \overline{p_\phi}(\mathbf{x})$$
(1.19)

In practice, none of the above moments are accessible to observations of LG galaxies. Instead (and only in the case where we apply these equations to luminous matter), only the projected radial position and the line-of-sight (LOS) velocity can be measured directly, i.e. without making model assumptions. The LOS

velocity is the velocity component parallel to the line of sight established between the distant observer on earth and the center of the observed galaxy (given that the galaxy is sufficiently far away for the LOS vector to be parallel to the vector connecting the distant observer on earth with any given star in the galaxy). Refer to figure 1.2 for a depiction of the relevant coordinates.

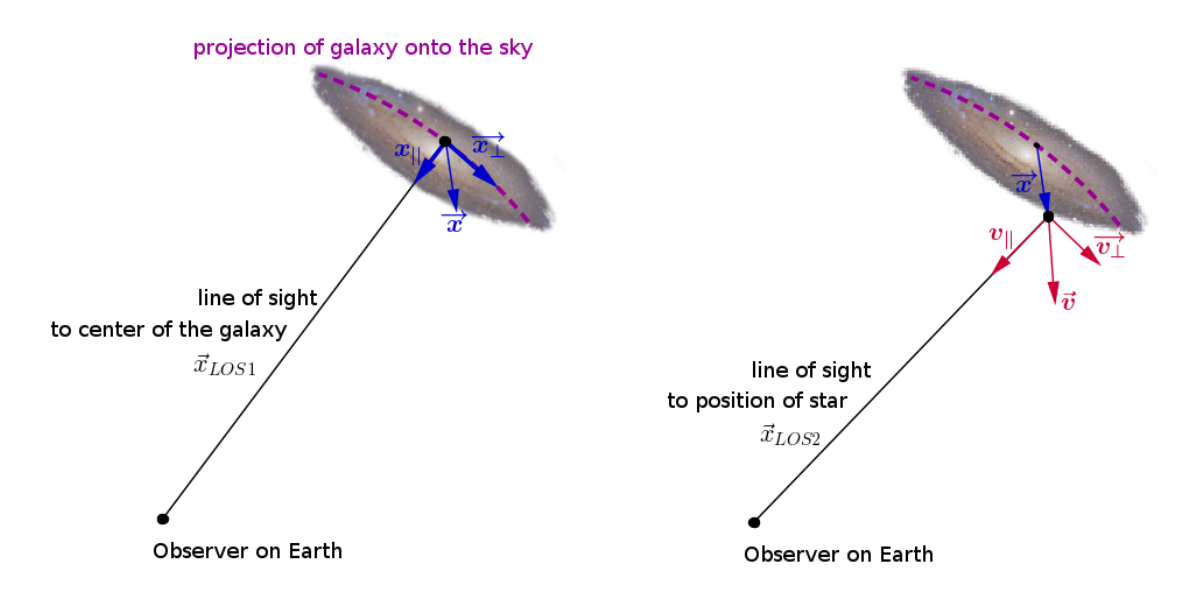


Figure 1.2: (left side) Definition of line of sight $(\vec{x_{||}})$ and projected (!) radial coordinate (x_{\perp}) , sometimes also R) of a position (\vec{x}) within the galaxy. Note that the actual radial coordinate r refers to the norm of the vector \vec{x} . r and R only coincide when a perfectly flat disk is viewed along the symmetry axis. (right side) Definition of line of sight $(\vec{v_{||}})$ and projected radial coordinate (v_{\perp}) , sometimes also v_R) of a velocity (\vec{v}) within the galaxy. Note that $\vec{x}_{LOS1} = \vec{x}_{LOS2}$ in the case of a distant galaxy. The background image of the Andromeda galaxy was taken from [12]

Since these LOS and projected radial positions are highly useful, their distribution function and most meaningful moments are defined below. Among them is the line-of-sight velocity distribution $P_{\mathbf{x}_{\perp}}(v_{||})$,

$$P_{\mathbf{x}_{\perp}}(v_{||}) = \frac{\int \nu(\mathbf{x}) dx_{||} \int d^2 v_{\perp} P_{\mathbf{x}}(\mathbf{v})}{\int \nu(\mathbf{x}) dx_{||}}$$
(1.20)

$$\overline{v_{||}}(x_{\perp}) = \int dv_{||}v_{||}P_{\mathbf{x}_{\perp}}(v_{||}) \tag{1.21}$$

$$\overline{v_{||}^2}(x_{\perp}) = \int dv_{||} v_{||}^2 P_{\mathbf{x}_{\perp}}(v_{||})$$
 (1.22)

$$\sigma_{||}^2 = \overline{v_{||}^2} - \overline{v_{||}}^2 \tag{1.23}$$

With the $\sigma_{||}$ as the line-of-sight velocity dispersion (also σ_{LOS}).

1.2 Jeans equations 15

1.2.3 Jeans equations

With these moments now defined, we are now ready to derive Jeans equations. Note that the number density $\rho(\mathbf{x})$ can be obtained from the spatial probability function $\nu(\mathbf{x})$ via $\rho(\mathbf{x}) = N\nu(\mathbf{x})$, with N as the total number of the component under consideration within the galaxy (e.g. total number of stars or total number of dark matter particles). This means, for DM particles $\rho_{DM}(\mathbf{x}) = N_{tot,DM} \cdot \nu_{DM}(\mathbf{x})$ and for stellar matter $\rho^*(\mathbf{x}) = N_{tot}^* \cdot \nu^*(\mathbf{x})$. We, therefore, elect to rewrite the equations using the more physically accessible number density instead of the spatial probability function. ‡ . In the following, spatial dependencies are implied, but not explicitly noted.

In Cartesian coordinates:

• 1st order Jeans equation, obtained by integrating equation (1.13) over d^3v

$$\frac{\partial}{\partial t} \int f d^3 v + \frac{\partial}{\partial x_i} \int f v_i d^3 v + \frac{\partial \Phi}{\partial x_i} \int \frac{\partial f}{\partial v_i} d^3 v = 0$$
 (1.24)

rewritten using the previously defined moments and with the vanishing boundary term

$$\frac{\partial}{\partial t}\rho + \frac{\partial}{\partial x_i}\overline{v_i}\rho = 0 \tag{1.25}$$

• 2nd order Jeans equation, obtained by integrating equation (1.13) over $v_r d^3 v$

$$\rho \frac{\partial \overline{v_j}}{\partial t} + \rho \overline{v_i} \frac{\partial \overline{v_j}}{\partial x_i} = -\rho \frac{\partial \Phi}{\partial x_j} - \frac{\partial (\rho \sigma_{ij}^2)}{\partial x_i}$$
 (1.26)

In spherical coordinates:

- 1st order Jeans equation, obtained by integrating equation (1.14) over d^3p evaluates to 0=0, as a consequence of uneven moments $(\overline{v_r}, \overline{v_\theta}, \overline{v_\phi})$ vanishing
- 2nd order Jeans equation, obtained by integrating equation (1.14) over $p_r d^3 p$ (see Appendix A)

[‡]Alternatively, we may also think of ρ as the mass density with $\rho(\mathbf{x}) = M\nu(\mathbf{x})$ and M as the total mass of the component under consideration within the galaxy [11, p359] (i.e. for dark matter particles $\rho_{DM}(\mathbf{x}) = M_{tot,DM} \cdot \nu_{DM}(\mathbf{x})$ and for stellar matter $\rho^*(\mathbf{x}) = M_{tot}^* \cdot \nu^*(\mathbf{x})$). This assumes that all particles/stars of the same component are identical, which is consistent with the initial assumptions made for the Boltzmann equations. The following analysis still applies, although adjustments may have to be made to recover correct dimensionality (e.g. Σ as the projected mass density instead of projected number density)

$$\frac{\partial}{\partial r}\overline{v_r^2}\rho + \rho\frac{\partial\Phi}{\partial r} + \frac{1}{r}\rho\overline{v_r^2}2(-\frac{\overline{v_\theta^2} + \overline{v_\phi^2}}{2\overline{v_r^2}} + 1) = 0$$

It is then useful to define the anisotropy parameter

$$\beta = -\frac{\overline{v_{\theta}^2} + \overline{v_{\phi}^2}}{\overline{2v_r^2}} + 1 \tag{1.27}$$

which generally is a function of position and heavily depends on the total angular momentum. Based on its range, one discerns between radially biased ($\beta > 0$) and tangentially biased ($\beta < 0$) models. Perfectly radial orbits correspond to $\sigma_{\theta} = \sigma_{\phi} = 0$ and $\beta = 1$, whereas perfectly circular orbits lead to $\sigma_{r} = 0$ and $\beta = -\infty$. $\beta = 0$ represents an ergodic system [11, p294]. This leads to the 2nd order Jeans equation in spherical coordinates (note that, since $\overline{v_{r}} = 0$, $\overline{v_{r}^{2}} = \sigma_{r}^{2}$):

$$\frac{\partial}{\partial r}(\overline{v_r^2}\rho) + \frac{2}{r}\rho\overline{v_r^2}\beta = -\rho\frac{\partial\Phi}{\partial r}$$
(1.28)

• 2nd order Jeans equation, obtained by integrating equation (1.14) over $p_{\phi}d^3p$

$$\frac{\partial}{\partial \phi} \overline{v_{\phi}^2} \rho - \frac{\partial \Phi}{\partial \phi} \rho = 0 \tag{1.29}$$

In spherically symmetric systems this will equate to 0=0

- 2nd order Jeans equation, obtained by integrating equation (1.14) over $p_{\theta}d^3p$ will also equate to 0=0 for spherically symmetric systems
- 4th order Jeans equation, obtained by integrating equation (1.14) over $p_r^3 d^3 p$

$$\left| \frac{\partial}{\partial r} (\rho \overline{v_r^4}) + \frac{2\beta'}{r} \rho \overline{v_r^4} + 3\rho \frac{d\Phi}{dr} \overline{v_r^2} = 0 \right|$$
 (1.30)

with
$$\beta'=1-rac{3}{2}rac{\overline{v_r^2v_t^2}}{\overline{v_r^4}}$$
 and $\overline{v_t^2}=\overline{v_\phi^2}+\overline{v_\theta^2}$

• combining the 4th order Jeans equations, obtained by integrating equation (1.14) over $p_r p_{\theta}^2 d^3 p$ and by integrating the same equation (1.14) over $p_r p_{\theta}^2 d^3 p$ gives

$$\boxed{4\rho\overline{v_r^2v_t^2} + r\frac{\partial}{\partial r}(\rho\overline{v_r^2v_t^2}) + \rho\frac{\partial\Phi}{\partial r}\overline{v_t^2}r - \rho\overline{v_t^4} = 0}$$
(1.31)

1.2 Jeans equations 17

Given that infinite order Jeans equations can be generated employing this mechanism of integrating equation (1.14) over momentum space, it is tempting to use this fact to write down just enough equations to solve the system, i.e. obtaining expressions for ρ and the moments of the velocity distribution function. However, as can be seen by comparing equations (1.28) and (1.30), higher order Jeans equations always introduce new variables (see table (1.2)), making it impossible to solve the system definitely via including higher order equations.

order	integral	equation	variables
1st order	d^3p	$0 = 0^{**}$	
2nd order	$p_r d^3 p$	$rac{\partial}{\partial r}\overline{v_r^2} ho + rac{2}{r} ho\overline{v_r^2}eta = - horac{\partial\Phi}{\partial r}$	$\rho, \overline{v_r^2}, \beta$
	$p_{\theta}d^3p$	$0 = 0^{**}$	
	$p_{\phi}d^3p$	$0 = 0^{**}$ $0 = 0^{**}$	
3rd order	$p_r^2 d^3 p$	$0 = 0^{**}$	
	$p_r p_t d^3 p$	$0 = 0^{**}$	
4th order	$p_r^3 d^3 p$	$\frac{\partial}{\partial r} \rho \overline{v_r^4} + \frac{2\beta'}{r} \rho \overline{v_r^4} + 3\rho \frac{d\Phi}{dr} \overline{v_r^2} = 0$	$\rho, \overline{v_r^4}, \overline{v_r^2}, \beta'$
	$p_r p_t^2 d^3 p$	$4\overline{v_r^2v_t^2} + \frac{r}{\rho}\frac{\partial}{\partial r}\rho\overline{v_r^2v_t^2} + \frac{\partial \Phi}{\partial r}\overline{v_t^2}r = \overline{v_t^4}$	$\rho, \overline{v_r^2 v_t^2}, \overline{v_t^2}, v_t^4$

Table 1.2: Overview of newly introduced variables per higher order Jeans equation.

** Due to spherical symmetry (No new equation, thus, no new introduced variables)

Commonly, these issues are circumvented by making assumptions about the system at hand. For example, constraining the system to those models that are perfectly isotropic lets us set β to 0 and effectively removes one of the variables. This is a frequent approach in literature, however, one runs risk to derive an inaccurate solution.

When working with real galactic systems such as dSphs, there are two main components to consider: the gravitationally dominating dark matter particles and the luminous tracers (e.g. stellar matter), both satisfying their own Jeans-equations. The total tracer mass is low compared to the total dark matter mass, meaning both components approximately move in the gravitational potential resulting from dark matter particles only (see [13]). The coupled Jeans-equations then read

$$\frac{\partial}{\partial r}(\overline{v_{r,DM}^2} \cdot \rho_{DM}) + \frac{2}{r}\rho_{DM} \cdot \overline{v_{r,DM}^2} \cdot \beta_{DM} = -\rho_{DM} \frac{\partial \Phi_{DM}}{\partial r}$$
(1.32)

$$\frac{\partial}{\partial r}(\overline{v_r^{*2}} \cdot \rho^*) + \frac{2}{r}\rho^* \cdot \overline{v_r^{*2}} \cdot \beta^* = -\rho^* \frac{\partial \Phi_{DM}}{\partial r}$$
 (1.33)

with the subscript DM indicating dark matter components and the superscript * indicating stellar components. Since Φ_{DM} can be constructed from ρ_{DM} , it is not an independent variable (see table 1.2). These equations bear similarity to the equation for hydrostatic equilibrium (see section 2.1.2). The analysis of dark matter and tracer components using line-of-sight velocity data and the previous Jeans-equations (including equation (1.34)) is referred to as *standard Jeans analysis*

1.2.4 Virial equations

Due to the previously mentioned limitations, the profiles suffer from *mass-anisotropy degeneracy* (also *density-anisotropy degeneracy* or β -*degeneracy*) (see e.g. [14], [15]): From measuring physical quantities, such as the line-of-sight velocity dispersion (see equation 1.34), one cannot clearly determine both the anisotropy parameter β and the velocity dispersion (or, equivalently, the enclosed mass or density). In order to try to alleviate this issue, the Virial equations are introduced in the following.

The solutions of Boltzmann equation are functions of momenta and positions which describe mass distributions and kinematics of the system. As we have seen in the previous chapter, Jeans equations are derived from Boltzmann equation by integrating momentum dependencies out. The solutions of Jeans equations are therefore profiles (e.g. mass profiles M(r)). Another measure is obtained by going a step further and integrating spatial dependencies out of the Jeans equations. The solutions of these new Virial equations are parameters, which won't allow for determining the profiles analytically, but may be used as fit parameters (see e.g. *Fairbairn et alii* [15]).

Before giving a derivation of the second order Virial equation, we will first introduce equation (1.34). This identity is given by *Binney et Tremaine* [11][16]

$$\Sigma(R)\overline{v_{LOS}^2(R)} = 2\int_R^\infty \left(1 - \beta(r)\frac{R^2}{r^2}\right) \frac{\rho(r)\overline{v_r^2(r)}r}{\sqrt{r^2 - R^2}} dr$$
 (1.34)

where $\Sigma(R)$ is the 2D number density as projected onto the sky, $\rho(r)$ the 3D stellar number density, R the 2D projected radius (see figure (1.2) for clarifications), and r the 3D radius. For a proof of this equation, see Appendix A.

Now to continue onto the Virial equations. Merrifield and Kent [17] show that the second order Virial equation reads

$$3 \int_0^\infty \Sigma(R) \overline{v_{LOS}^2(R)} R dR = 2 \int_0^\infty \rho(r) \frac{d\Phi(r)}{dr} r^3 dr$$
 (1.35)

The usefulness of this equation is immediately clear once the left-hand side is examined: It is a function of quantities that can be directly accessed via observation only.

Proof. Comparing the Virial equation to the 2nd order Jeans equation, suggests that equation (1.28) ought to be multiplied with r^3 and integrated over all spatial coordinates to yield:

 $[\]S$ It will become apparent that we are looking at the Jeans equation describing the tracer component - equation 1.33, since this component is the only one directly accessible to observation. Virial equations relate observationally determined quantities to the underlying profiles. The tracer particles move in the dark matter particle potential Φ , which we will assume to be known in the following

1.2 Jeans equations 19

$$\int \frac{\partial}{\partial r} (\overline{v_r^2} \rho) r^3 dr + \int \frac{2}{r} \rho \overline{v_r^2} \beta r^3 dr = -\int \rho \frac{\partial \Phi}{\partial r} r^3 dr
-3 \int \overline{v_r^2} \rho r^2 dr + 2 \int \rho \overline{v_r^2} \beta r^2 dr = -\int \rho \frac{\partial \Phi}{\partial r} r^3 dr
\int \overline{v_r^2} \rho r^2 (2\beta - 3) dr = -\int \rho \frac{\partial \Phi}{\partial r} r^3 dr$$
(1.36)

Multiplying equation (1.34) with R and integrating both sides from R = 0 to ∞ (this is, again, motivated by comparing the left-hand sides of equation (1.35) and equation (1.34)):

$$\int_{R=0}^{\infty} \Sigma \overline{v_{LOS}^{2}(R)} R dR = 2 \int_{R=0}^{\infty} \int_{r=R}^{\infty} (1 - \beta \frac{R^{2}}{r^{2}}) \frac{\rho \overline{v_{r}^{2}} r}{\sqrt{r^{2} - R^{2}}} R dr dR
= 2 \int_{r=0}^{\infty} \int_{R=0}^{r} (1 - \beta \frac{R^{2}}{r^{2}}) \frac{\rho \overline{v_{r}^{2}} r}{\sqrt{r^{2} - R^{2}}} R dr dR
= 2 \int_{r=0}^{\infty} \rho \overline{v_{r}^{2}} r dr \int_{R=0}^{r} \frac{(1 - \beta \frac{R^{2}}{r^{2}})}{\sqrt{r^{2} - R^{2}}} R dR
= 2 \int_{r=0}^{\infty} \rho \overline{v_{r}^{2}} r (r - \frac{2}{3}\beta r) dr
= -\frac{2}{3} \int_{r=0}^{\infty} \rho \overline{v_{r}^{2}} r^{2} (2\beta - 3) dr$$
(1.37)

With this, equation (1.36) can be rewritten as

$$\frac{3}{2} \int_0^\infty \Sigma \overline{v_{LOS}^2} R dR = \int_0^\infty \rho \frac{\partial \Phi}{\partial r} r^3 dr \tag{1.38}$$

Not only does the second order Virial equation relate observationally accessible quantities to the profiles we want to probe, it also has the added advantage that it, compared to the same order Jeans equation, reduces the amount of unknown variables involved. The same goes for the two relevant fourth order Jeans equations (given by [17]):

$$\left| \int_0^\infty \Sigma \overline{v_{LOS}^4} R dR = 2 \int_0^\infty \rho \overline{v_r^2} \left(1 - \frac{2}{5} \beta \right) \frac{d\Phi}{dr} r^3 dr \right|$$
 (1.39)

$$\int_0^\infty \Sigma \overline{v_{LOS}^4} R^3 dR = 2 \int_0^\infty \rho \overline{v_r^2} \left(1 - \frac{6}{7} \beta \right) \frac{d\Phi}{dr} r^5 dr$$
 (1.40)

Table (1.3) shows how introduction of Virial equations reduces the number of unknown variables ($\Sigma(R)$ and moments of the line-of-sight velocity distribution

Jeans equation Virial equation
$$1^{st} \quad \text{equ.} \quad \frac{\partial}{\partial r}(\overline{v_r^2}\rho) + \frac{2}{r}\rho\overline{v_r^2}\beta = -\rho\frac{\partial\Phi}{\partial r} \quad \rightarrow \quad 3\int_0^\infty \Sigma \overline{v_{LOS}^2}RdR = 2\int_0^\infty \rho\frac{d\Phi}{dr}r^3dr \\ \quad \text{var.} \quad \rho, \overline{v_r^2}, \beta \qquad \qquad \rho \\ 2^{nd} \quad \text{equ.} \quad \frac{\partial}{\partial r}(\rho\overline{v_r^4}) + \frac{2\beta'}{r}\rho\overline{v_r^4} + 3\rho\frac{d\Phi}{dr}\overline{v_r^2} = 0 \quad \rightarrow \quad \int_0^\infty \Sigma \overline{v_{LOS}^4}R^3dR = 2\int_0^\infty \rho\overline{v_r^2}\left(1 - \frac{6}{7}\beta\right)\frac{d\Phi}{dr}r^5dr \\ \quad \text{var.} \quad \rho, \overline{v_r^4}, \beta', \overline{v_r^2} \qquad \qquad \rho, \beta, \overline{v_r^2}$$

Table 1.3: comparison of equations and variables for Jeans equations and Virial equations of the same order

are not considered unknown, because they can be fixed by observations). Specifically, an n-order Virial equation contains only those variables that are already present in the (n-2)-order Jeans equation. However, despite their many advantages, it should be noted that Virial equations can't be used to solve the system either, as their derivation calls for the profiles' spatial dependencies to be integrated out, yielding only parameters. Nevertheless, these parameters are very useful for the purpose of fitting and comparing the quality of different proposed density and velocity anisotropy profiles. [15]



Dark Matter Density Models

As previously stated, solving a model describing dSPhs is equivalent to finding a characteristic density distribution and the moments of the velocity distribution function. The following proposed models represent attempts at finding these solutions. The final goal in this context is to find a lower bound to the dark matter particle mass using methods such as the Tremaine Gunn bound.

2.1 Randall-Scholtz-Unwin Model

This model will be referred to as Randall-Scholtz-Unwin (RSU) Model, after its originators. We will first reiterate its derivation (found in [18]) and go into detail about the model's issues after.

To summarize, the RSU model introduces a two parameter dark matter density profile, by assuming:

- the body under consideration is a dark matter dominated object with spherical symmetry
- Observational knowledge of the half-light mass $M_{1/2}$ enclosed within half light radius $r_{1/2}$ (see Chapter (1.1)).
- Study of isotropic and collisionless dark matter as ideal gas
 - Temperatures of particles defined by Virial condition (finite orbits)
 - Pressure increased by Fermi degeneracy pressure
- Observational knowledge of the core radius R_c where $\frac{dlog\rho}{dlogR} = -\frac{3}{2}$

2.1.1 Model

Following [18], as starting point, one chooses to consider the collection of dark matter particles only, which dominates the total mass of the dSPh as a though it

were a perfect fluid in hydrostatic equilibrium (more about this choice in chapter (2.1.2)). The hydrostatic equilibrium equation then reads :

$$\frac{dP(r)}{dr} = -\left(\frac{GM(r)}{r^2}\right)\rho(r) \tag{2.1}$$

where $\rho(r)$ describes the dark matter matter density (i.e. $\rho=\rho_{DM}$) and with the enclosed mass

$$M(r) = 4\pi \int_0^r \rho(r')r'^2 dr'$$
 (2.2)

noting that M(0) = 0. An equation of state is required to solve the system. The RSU-model's authors consider the pressure in two regimes within the galaxy, with the total pressure resulting from effects in both the quantum and classical regime approximated by $P(r) = P_{class}(r) + P_{quantum}(r)$. The classical pressure is derived from the Virial condition, which, for finite orbits in a stable gravitationally bound system, can be expressed as:

$$\overline{E_{kin}}(r) = \frac{GM(r)m}{2r}
\rightarrow T = \frac{GM(r)m}{2r}
\rightarrow P_{class}(r) = \frac{\rho(r)}{m}T(r) = \frac{GM(r)\rho(r)}{2r}$$
(2.3)

The Fermi degeneracy pressure is that of a fully degenerate gas at T=0. This pressure is consequence of the Pauli exclusion principle, which acts as a force resisting the compression of matter into a smaller phase space volume. The quantum pressure term is given by [19, p197]:

$$P_{quantum}(r) = \frac{2}{3} \frac{E_{tot,quantum}|_{T=0}}{V}$$
 (2.4)

$$=\frac{(3\pi^2)^{2/3}\hbar^2}{5m^{8/3}}\rho(r)^{5/3} \tag{2.5}$$

The two pressure terms enable rewriting of equation (2.10)

$$\frac{\partial}{\partial r} \left(\frac{GM(r)\rho(r)}{2r} + \frac{(3\pi^2)^{2/3}\hbar^2}{5m^{8/3}} \rho(r)^{5/3} \right) = -\rho(r) \frac{GM(r)}{r^2}$$
 (2.6)

which, together with equation (2.2), results in a system of equations, which can be solved for $\rho(r)$. The solution has two degrees of freedom: the core density $\rho(r=0)=\rho_0$ and the particle mass m. As stated in chapter (1.1), the mass enclosed within the half light radius $r_{1/2}$ is assumed to be highly model independent. $M(r_{1/2})$ can, therefore, be used to fix the one free parameters left after the other has been specified (see figure (2.1).

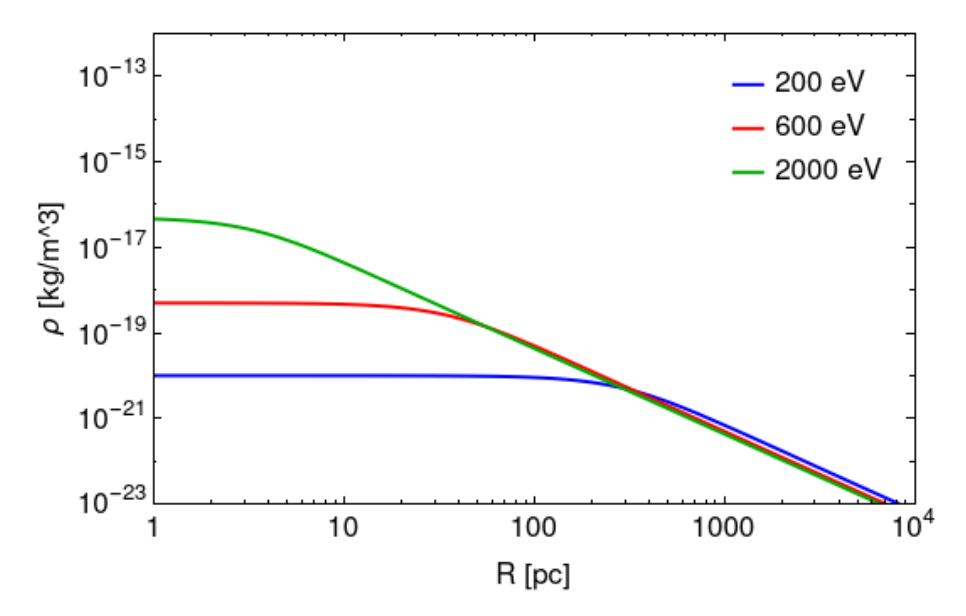


Figure 2.1: density profiles of the RSU model for a particle with one degree of freedom. The (ρ_0,m) -pairs were chosen such that they reproduce the mass enclosed within the half-light radius of the Fornax LG dSph.

Mass bound

With another measure, similar to $r_{1/2}$, one can now uniquely fix the parameter pair (ρ_0 ,m). The authors of the RSU-model choose the core radius of the galaxy under consideration (for issues regarding this choice see chapter 2.1.2), as defined by:

$$\left. \frac{dlog\rho}{dlogR} \right|_{R=R_c} = -\frac{3}{2} \tag{2.7}$$

The blue curve in figure (2.2) shows possible values of the core radius R_c for density profiles that all reproduce the correct half-light mass $M_{1/2}$ with varying particle mass m. The red curve segment shows the 95% confidence interval for the core radius for the Fornax LG dSph as determined by [20].

$$R_c = 1_{0.4}^{0.8} \,\text{kpc} \tag{2.8}$$

The upper limit for the core radius determines the lower mass bound. The authors of the RSU-model thus derive a lower mass bound of 70 eV. For the reproduction here, a less strict lower mass bound of 55 eV was derived. The difference is assumed to be due to different methods used to determine the accurate (ρ_0, m) -pair to reproduce $M_{1/2}$. Both estimates are considerably lower than those based on the Tremaine-Gunn bound (see Table (1.1)).

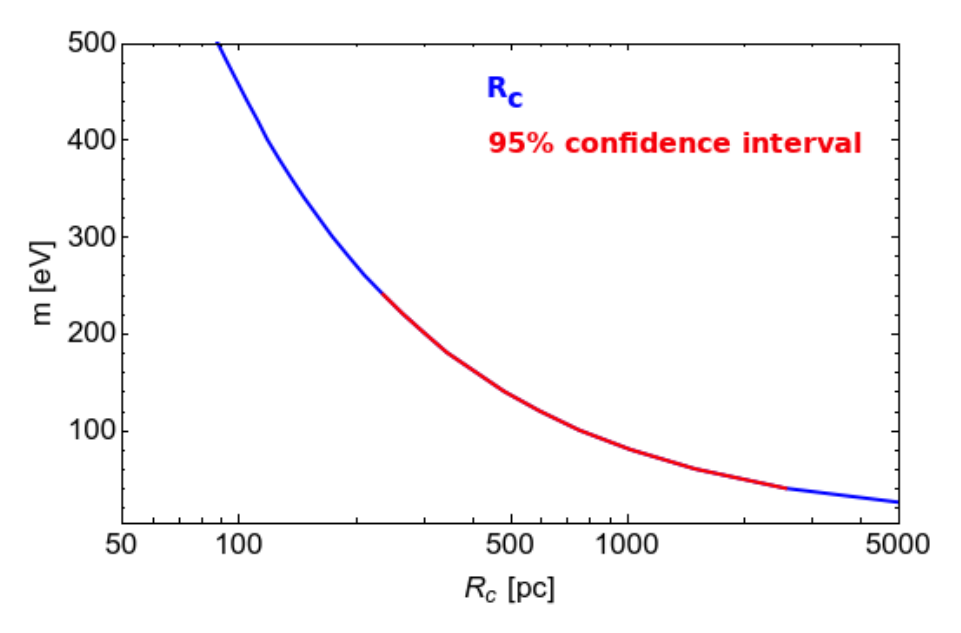


Figure 2.2: dark matter particle mass as a function of core radius for a particle with one degree of freedom

2.1.2 Limitations

Using the hydrostatic equilibrium equation (2.1) to describe the dark matter density profile, implicitly implies for the anisotropy parameter $\beta(r)=0$. We will prove this by showing that this equation is equivalent to the one derived for a static, spherically symmetric, and isotropic ideal gas. Firstly, one refers to the spherical second order Jeans equation, derived in chapter (1.2.3). Here, ρ refers to the matter density, instead of the number density - see footnote on page 15. Contrary to other models, this derivation disregards the existence of any tracer populations in the dSphs and instead only looks at dark matter particles.

$$\frac{\partial}{\partial r}(\overline{v_r^2}\rho) + \frac{2}{r}\rho\overline{v_r^2}\beta = -\rho\frac{\partial\Phi}{\partial r}$$
 (2.9)

To get to equation (2.1), the RSU model implicitly assumes that the system is isotropic, yielding $\beta=0$. Furthermore the system of dark matter particles is supposed to behave as an ideal gas, with the ideal gas law PV=NT ($c=k_B=1$) or $Pm=\rho T$ with m as the dark matter particle mass. The stars are then Boltzmann-distributed with a rms velocity of $\overline{v^2}=\frac{3T}{m}\to \overline{v_r^2}=\frac{T}{m}$ The second order Jeans equation thus becomes

$$\frac{\partial}{\partial r} \left(\frac{T(r)}{m} \cdot \frac{P(r)m}{T(r)} \right) = -\rho(r) \frac{\partial \Phi(r)}{\partial r}$$

$$\frac{\partial}{\partial r} P(r) = -\rho(r) \frac{GM(r)}{r^2}$$
(2.10)

Setting $\beta = 0$ is consistent with the claim of ergodicity (see chapter (1.2.3)),

which is necessary for the Virial theorem to be applicable.*

Restricting the dark matter particles to an isotropic velocity dispersion across the entire radial range is very limiting and may not describe real cases accurately (e.g. [15] for Sculptor or [21] for Sculptor and Fornax). Apart from this issue, the core radius R_c is highly model dependent and has been derived specifically for Burkert and NFW density profiles, which are naturally different from those of the RSU-model, impacting the accuracy of the mass bound.

2.2 Ruffini-Argüelles-Rueda Model

The Ruffini-Argüelles-Rueda (RAR) Model is a dark matter halo model modified by three free parameters. Like before, we will first cover their derivation (based on [22],[23]) and then analyse the fundamental issues associated with this theory. To summarize, the RAR dark matter density profile assumes:

- Thermodynamic equilibrium/ reversible changes
- Perfect fluid in static, spherically symmetric metric (leading to Tolman-Oppenheimer-Volkhoff equation for hydrostatic equilibrium)
- Pressure P and energy density ρ defined by Fermi statistics
- Evaluation in rest frame of the fluid

2.2.1 Model

Similarly, to the Randall-Scholtz-Unwin Model, the RAR-model primarily considers the behaviour of the dark matter component in the galaxy and disregards the tracer population (i.e. $\rho = \rho_{DM}$). The theory behind the RAR model is built upon the work done by *O. Klein* [24], who derives expression (2.19) and (2.20) the following way (only for the derivation of these two expressions will we use c=1). As starting-point, one chooses the energy momentum tensor for the perfect fluid:

$$T^{\mu\nu} = (P + \rho_e)u^{\mu}u^{\nu} - Pg^{\mu\nu}$$
 (2.11)

with a energy density ρ_e , pressure P, and fluid 4-velocity u^{μ} . A very general spherically symmetric metric describing the gravitational field of a galaxy can be written down:

$$ds^{2} = e^{\nu(r)}dt^{2} - e^{\mu(r)}(dr^{2} + r^{2}d\Omega^{2})$$
(2.12)

^{*}The Virial theorem dictates $\overline{v^2} \frac{m}{2} = \overline{E_{kin}}(r) = \frac{GM(r)m}{2r}$. Therefore, since $\overline{v^2} = \frac{3T}{m}$, we have $T = \frac{GMm}{3r}$. The factor of 1/3 instead of 1/2, as used by the authors of the RSU-model, does not change the model fundamentally and has little influence on the derived lower mass bound

As is a typical assumption, we are considering the fluid in its rest frame (expectation values $\overline{v} = 0$). Conservation of energy-momentum yields:

$$T^{\mu\nu}_{;\mu} = 0$$

$$((P + \rho_e)u^{\mu}u^{\nu})_{;\mu} + (Pg^{\mu\nu})_{;\mu} = 0$$

$$\Gamma^{\mu}_{\sigma\nu}(P + \rho_e)u^{\sigma}u^{\nu} + \partial^{\nu}P = 0$$

$$\partial_i P + \frac{P + \rho_e}{2}\partial_i \nu(r) = 0$$
(2.13)

From thermodynamic principles, we have, for a closed system and reversible changes (with chemical potential μ and entropy S):

$$U = TS - PV + \mu N$$

$$dU = TdS - PdV + \mu dN$$

$$\downarrow$$

$$0 = SdT - VdP + Nd\mu$$

$$0 = \left(\frac{U + PV - \mu N}{T}\right) dT - VdP + Nd\mu$$
(2.14)

Which we can use to derive (with $\eta = N/V$, energy density $\rho_e = U/V$):

$$\frac{\nabla_i T}{T} (\rho_e + P - \mu \eta) - \nabla_i P + \eta \nabla_i \mu = 0$$
 (2.15)

With equation (2.13), this can be rewritten as

$$\left(\frac{\nabla_i T}{T} + \frac{\nabla_i \nu}{2}\right) (\rho_e + P) + \left(\frac{\nabla_i \mu}{\mu} - \frac{\nabla_i T}{T}\right) \eta \mu = 0 \tag{2.16}$$

Assuming $(\rho_e + P)$ and η to be linearly independent from each other (more about this in 2.2.2), equation (2.16) yields two separate equations:

$$\left(\frac{\nabla_i T}{T} + \frac{\nabla_i \nu}{2}\right) = 0 \tag{2.17}$$

$$\left(\frac{\nabla_i \mu}{\mu} - \frac{\nabla_i T}{T}\right) = 0 \tag{2.18}$$

which can be solved to give:

$$T = T_0 e^{\frac{\nu_0 - \nu}{2}} \tag{2.19}$$

$$\mu = \mu_0 e^{\frac{\nu_0 - \nu}{2}} \tag{2.20}$$

With these two equations derived, the authors of the RAR model refer to the Tolman–Oppenheimer–Volkoff equation [25]:

$$\frac{d\nu}{dr} = 2\frac{2GM(r)c^2 + \frac{4\pi Gr^3 P(r)}{c^4}}{r^2 \left(1 - \frac{2GM(r)}{c^2 r}\right)}$$
(2.21)

derived, again, for a perfect fluid in a static, spherically symmetric metric by solving Einstein's field equations.

Since the dark matter particles are assumed to be fermionic, it is appropriate to use the Fermi-Dirac distribution f(E) function to describe their velocity distribution, as well as pressure P and density ρ [26] [†]

$$f(p,r) = \frac{1}{1 + Exp\left(\frac{E(p)}{kT(r)} - \frac{\mu(r)}{kT(r)}\right)}$$

$$\rho(r) = 2\frac{1}{h^3} \int f(p,r)E(p)d^3p$$

$$P(r) = 2\frac{c^2}{3h^3} \int f(p,r)\frac{p^2}{E(p)}d^3p$$
(2.22)

Rescaling of the system's variables makes it more clear and simpler to solve:

$$\hat{M} = Mm^2 \sqrt{2 \left(\frac{G}{hc}\right)^3}$$

$$\hat{P} = P \frac{h^3}{2m^4 c^5}$$

$$\hat{\rho} = \rho \frac{h^3}{2m^4 c^3}$$

$$\hat{r} = rm^2 \sqrt{\frac{2Gc}{h^3}}$$
(2.23)

Besides this, one also defines

$$\beta(r) = \frac{kT(r)}{mc^2} \tag{2.24}$$

$$\theta(r) = \frac{\mu(r)}{kT(r)} \tag{2.25}$$

(β is not to be confused with the velocity anisotropy) which one can rewrite, using equations (2.19) and (2.20):

$$\beta(r) = \frac{kT_0}{mc^2} e^{\frac{\nu(r) - \nu_0}{2}} = \beta_0 e^{\frac{\nu(r) - \nu_0}{2}}$$
(2.26)

$$\theta(r) = const = \theta_0 \tag{2.27}$$

Finally, one can rewrite the Tolman–Oppenheimer–Volkoff equation (2.21) and the distribution function equations (2.22) with the rescaled variables:

[†]The authors of the RAR-model choose a slightly different definition for the chemical potential μ than the one used here. Changing from μ_{RAR} to the variable μ used here, is done simply via $\mu_{RAR} = \mu - mc^2$ (Ruffini et alii further redefine the Fermi-Dirac distribution such that the result of the derivation is unchanged). Some calculations are more instructive and simpler using the notation presented here.

$$\frac{d\nu}{d\hat{r}} = 2\frac{\hat{M}(\hat{r}) + 4\pi\hat{r}^3\hat{P}(\hat{r})}{\hat{r}\left(\hat{r} - 2\hat{M}(\hat{r})\right)}$$
(2.28a)

$$\hat{\rho}(\nu(\hat{r})) = 4\pi \int f(p,\nu(\hat{r})) p^2 \sqrt{1+p^2} dp$$
 (2.28b)

$$\hat{P}(\nu(\hat{r})) = \frac{4\pi}{3} \int f(p, \nu(\hat{r})) \frac{p^4}{\sqrt{1+p^2}} dp$$
 (2.28c)

$$f(p,\nu(\hat{r})) = \left(1 + Exp\left(\frac{\sqrt{1+p^2}}{\beta(\nu(\hat{r}))} - \theta_0\right)\right)^{-1}$$
 (2.28d)

In accordance with the weak-field approximation, $v_0 = v(r = 0)$ is chosen to be 0. The free parameters are then m, β_0 and θ_0 . Together with the usual expression for the enclosed mass

$$\frac{d\hat{M}(\hat{r})}{d\hat{r}} = 4\pi\hat{r}^2\hat{\rho}(\hat{r}) \tag{2.29}$$

The system of equations (2.28) can be solved numerically upon choice of parameters (β_0 , θ_0). After solving the system, the thus obtained quantities can be rescaled back to physical units. The parameter m is only used to rescale the system and is not necessary to specify to obtain the initial solution. The resulting density profile is given in figure (2.3). It is marked by three distinct region: A quantum core (here, up until 0.1 pc), a transition regime, where the density profile sharply drops and eventually plateaus, and a classical regime, where quantum corrections are negligible and which is described by Boltzmann statistics, with a isothermal sphere ($\rho \sim r^{-2}$).

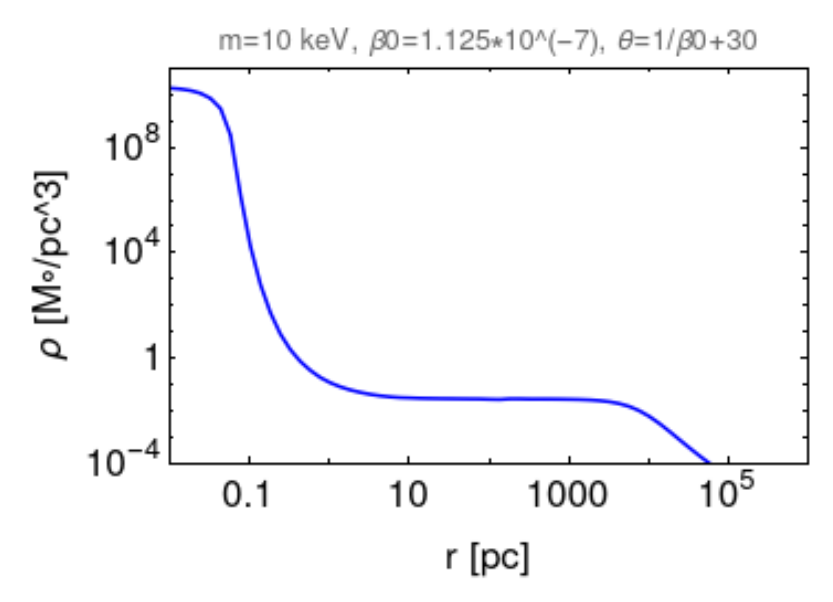


Figure 2.3: Density profile of the RAR model. ‡

The free parameters may be chosen such that observational quantities are reproduced. Figure (2.3)) suggests how the free parameter of the fermion particle mass may be fixed via comparison to the value of $M_{1/2}$ or to the circular velocity $v_{1/2}$ defined as

$$v_{1/2} = \sqrt{\frac{GM(r)}{r - 2GM(r)/c^2}}$$
 (2.30)

For fixed $\beta_0 = 1.3 * 10^{-7}$, $\theta = 1/\beta_0 + 25$, variation of the parameter m leads to different values for the enclosed mass $M_{1/2}$ within the half-light radius $r_{1/2}$ (red curve) or $v_{1/2}$ (blue curve). The curves are normalized such that a value of 1 (grey line) represents a typical measured value (here for spiral galaxies, as given by *Ruffini et alii* [22] and *Blok et alii* [27]).

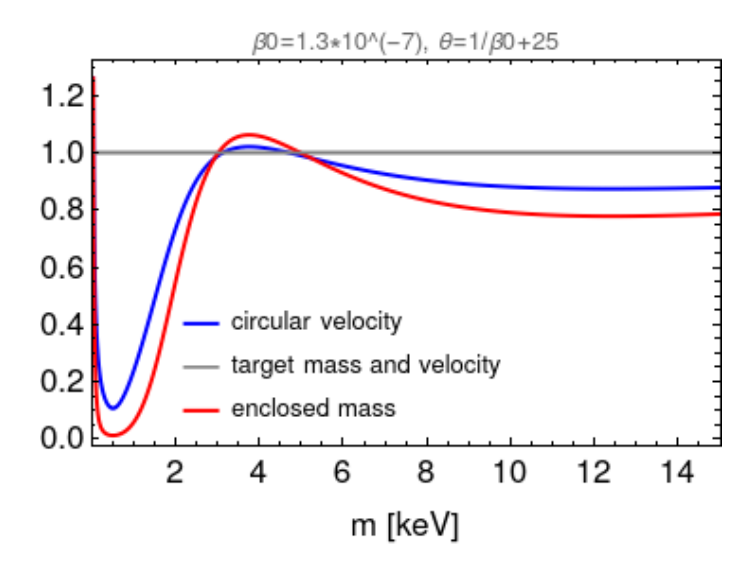


Figure 2.4: Enclosed mass $M_{1/2}$ at the half-light radius (red curve) and circular velocity $r_{1/2}$ (blue curve) for different fermion particle masses m, normalized such that a value of 1 corresponds with the observationally obtained value. This means that, for the given parameters (β_0, θ_0) , a particle mass of 2.5keV or 4.5keV is predicted

Scaling

A few words on scaling of the density profile: The particle mass m only influences overall scale. This is because the mass is not used to solve the (dimensionless) differential equation, and is instead only relevant for rescaling back to physical units. The r-axis scales like m^{-2} (i.e. a higher particle mass means the density profile falls of quicker) and the ρ -axis as m^4 (i.e. a higher particle mass means the density is higher). Variation of β_0 seems to mostly result in a change in the

[‡]Due to varying notation, for $\theta_{RAR,0}=30$ we have $\theta=\frac{\mu_0}{kT_0}=\frac{\mu_{RAR,0}}{kT_0}+\frac{1}{\beta_0}=\theta_{RAR,0}+\frac{1}{\beta_0}=30+\frac{1}{\beta_0}$

overall scale, with higher densities for larger β_0 . The influence of θ_0 is clear upon comparison (see 2.5): The lower θ_0 the larger the classical regime.

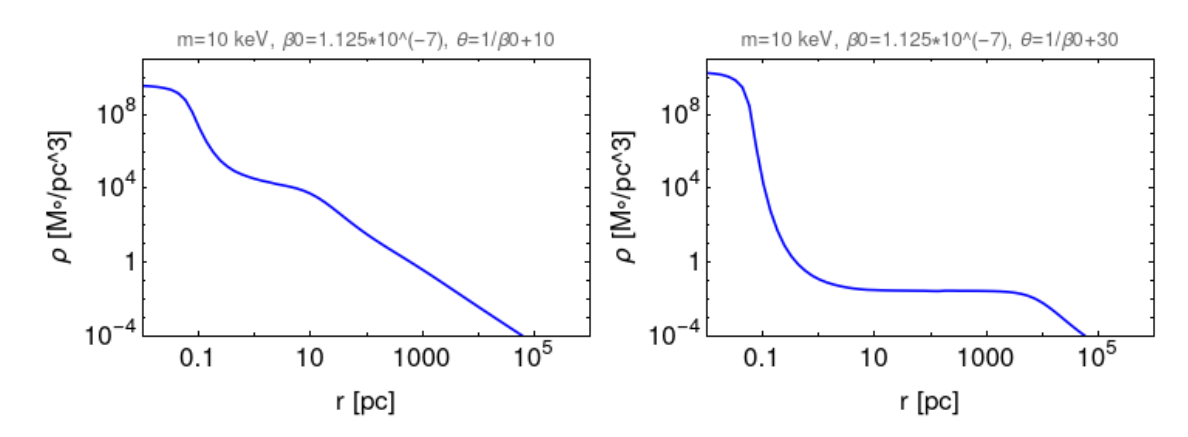


Figure 2.5: density profiles for variation of θ_0 . (left) $\theta_0 = 1/\beta_0 + 10$, (right) $\theta_0 = 1/\beta_0 + 30$. The lower θ_0 the smaller the transition (flat) regime, and the larger the classical regime.

2.2.2 Limitations

Non-relativistic approximation

Due to the initial conditions used by *Ruffini et alii* ($\beta_0 \sim 10^{-7}$, $\theta_0 \sim 10^7$), $\nu(r)$ is small across the entire range ($\nu(r) < 10^{-5}$). Therefore, f(p) as defined by equation (2.28d), gets very small for large p ($f(0.007) \sim 10^{-94}$ for these values). For terms occurring inside this integrals one then has

$$p^2 \ll m^2 \qquad \sqrt{1+p^2} \approx 1 \qquad p^2 + p^4 \approx p^2$$
 (2.31)

Which reduces the important definitions

$$\hat{\rho}_{e}(\nu(\hat{r})) = 4\pi \int f(p,\nu(\hat{r}))p^{2}\sqrt{1+p^{2}}dp$$

$$\approx 4\pi \int f(p,\nu(\hat{r}))p^{2}dp$$

$$= \hat{\rho}_{m}(\nu(\hat{r}))$$
(2.32)

$$\hat{P}(\nu(\hat{r})) = \frac{4\pi}{3} \int f(p,\nu(\hat{r})) \frac{p^4}{\sqrt{1+p^2}} dp$$

$$\approx \frac{4\pi}{3} \int f(p,\nu(\hat{r})) p^4 dp$$

$$\ll \hat{\rho}_e(\nu(\hat{r}))$$
(2.33)

And since (with $\hat{\rho}_m = m\hat{\eta} \rightarrow \hat{\rho}_m = \hat{\eta}$).

$$\hat{\rho}_m(\nu(\hat{r})) = \hat{\eta}_e(\nu(\hat{r})) = 4\pi \int f(p,\nu(\hat{r})) p^2 dp \approx \hat{\rho}_e(\nu(\hat{r}))$$
 (2.34)

In other words: For ρ_m to be equal to ρ_e , $P + \rho$ has to be qual to ρ to the same order. Even without solving the system, one can see that *Ruffini et alii* explicitly assume $\rho_m = \rho_e$, since equation (2.28b) and equation (2.29) use the same definition for ρ . The equation

$$\partial_i \hat{P} = -\frac{\hat{P} + \hat{\rho}}{2} \partial_i \hat{v}(\hat{r}) \tag{2.35}$$

was derived using GR for a perfect fluid only. In their following derivation, *Ruffini et alii* [22], as well as *Gao et alii* [23], apply the relations to an ideal Fermi gas. To verify equation (2.35)s validity for a Fermi gas, we have to evaluate the equality using the integrals defined by equations (2.22). We do this by referring to figure (2.6), which shows different ways of arriving at a value for the pressure gradient $\frac{dP}{dr}$ by varying the value of \hat{v} (the precise functional dependence is unimportant, as we will show below).

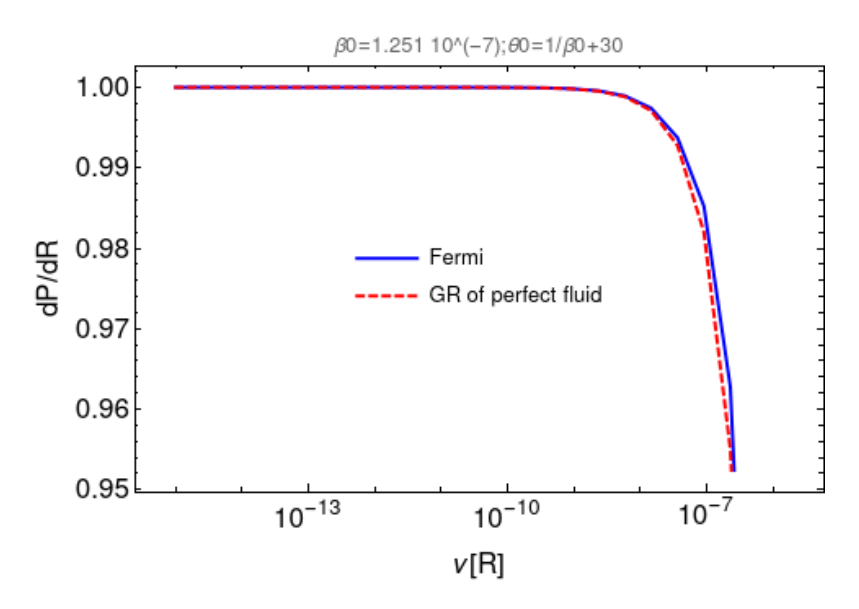


Figure 2.6: Comparisons of the (normalized) value for the pressure gradient (for specific values (θ_0, β_0) and varying v(r)) between Fermi and GR derivations. The curves seem to coincide (in our bona fide approach, small deviations are deemed acceptable)

The blue curve, i.e. the "Fermi" curve, is obtained by directly taking the derivative of

$$\hat{P}(\nu(\hat{r})) = \frac{4\pi}{3} \int f(p, \nu(\hat{r})) \frac{p^4}{\sqrt{1+p^2}} dp$$
 (2.36)

which is the definition of rescaled pressure for a Fermi gas. Since the coordinates are rescaled, one can disregard the value of m. Functionally, the equation depends on \hat{r} only through $\hat{v}(\hat{r})$, resulting in an unknown factor of $\hat{v}'(\hat{r})$ from the chain rule. Since the right-hand side of equation (2.35), conveniently, depends on $\hat{v}'(\hat{r})$ as well, one can simply eliminate this factor.

The red curve, i.e. "GR" curve, is obtained by plugging in the two definitions:

$$\hat{\rho}(\nu(\hat{r})) = 4\pi \int f(p,\nu(\hat{r})) p^2 \sqrt{1 + p^2} dp$$
 (2.37)

$$\hat{P}(\nu(\hat{r})) = \frac{4\pi}{3} \int f(p, \nu(\hat{r})) \frac{p^4}{\sqrt{1+p^2}} dp$$
 (2.38)

into the right-hand side of equation (2.35).

The variable $\hat{v}(\hat{r})$ is varied within a range consistent with the non-relativistic approximation and in order to eliminate any erroneous prefactors, both curves are normalized. For the GR formula to hold for the Fermi case, the two should be the same for every relevant \hat{v} . It seems like this condition is satisfied.

As we already saw, in this approximation $\hat{\rho}_e = \hat{\rho}_m$, which *Ruffini et alii* use to derive the equations (2.19) and (2.20). To summarize

$$\hat{P}(\nu(\hat{r})) \ll \hat{\rho}_e(\nu(\hat{r})) \tag{2.39}$$

$$\hat{\rho}_m(\nu(\hat{r})) = \hat{\eta}(\nu(\hat{r})) \approx \hat{\rho}_e(\nu(\hat{r})) = \hat{\rho}(\nu(\hat{r}))$$
(2.40)

By inserting these identities into equation 2.16, one obtains:

$$\left(\frac{\nabla_{i}T}{T} + \frac{\nabla_{i}\nu}{2}\right)(\hat{\rho} + \hat{P}) + \left(\frac{\nabla_{i}\hat{\mu}}{\hat{\mu}} - \frac{\nabla_{i}T}{T}\right)\hat{\eta}\hat{\mu} = 0$$

$$\left(\frac{\nabla_{i}T}{T} + \frac{\nabla_{i}\nu}{2}\right)\hat{\rho} + \left(\frac{\nabla_{i}\hat{\mu}}{\hat{\mu}} - \frac{\nabla_{i}T}{T}\right)\hat{\rho}\hat{\mu} = 0$$

$$\frac{\nabla_{i}T}{T} + \frac{\nabla_{i}\nu}{2} + \nabla_{i}\hat{\mu} - \frac{\nabla_{i}T}{T}\hat{\mu} = 0$$
(2.41)

with $\hat{\mu} = \frac{\mu}{mc^2}$. An important step in the derivation of *Ruffini et alii* was that ρ , P and η are linearly independent, which is not the case in this approximation and we don't get two independent equations.

General case

We have seen, that the non-relativistic approximation leads to contradictions which cannot bee remedied. Even though there is implicit proof for the idea that *Ruffini et alii* do work with this approximation, we will try to examine the derivation for a model not limited to a specific domain (as one can naively guess that P and ρ , based on their functional form introduced by equation (2.22), ought to be linearly independent in this case). The precise form of the density profiles might

look differently, but the system of equations used would only need to be adjusted slightly.

Figure (2.7) is equivalent to figure (2.6), but for the general case: The blue curve is, again, obtained by directly taking the derivative of the pressure (as defined by 2.38). The red curve is a result of plugging the two definitions for pressure and density (as defined by 2.38 and 2.37) into the right-hand side of

$$\partial_i \hat{P} / \partial_i \hat{v}(\hat{r}) = -\frac{\hat{P} + \hat{\rho}_e}{2} \tag{2.42}$$

The curves are normalized to intersect at v[r] = 0.1, to account for any erroneous prefactors. If the approach by *Ruffini et alii* is correct, the two curves should be identical.

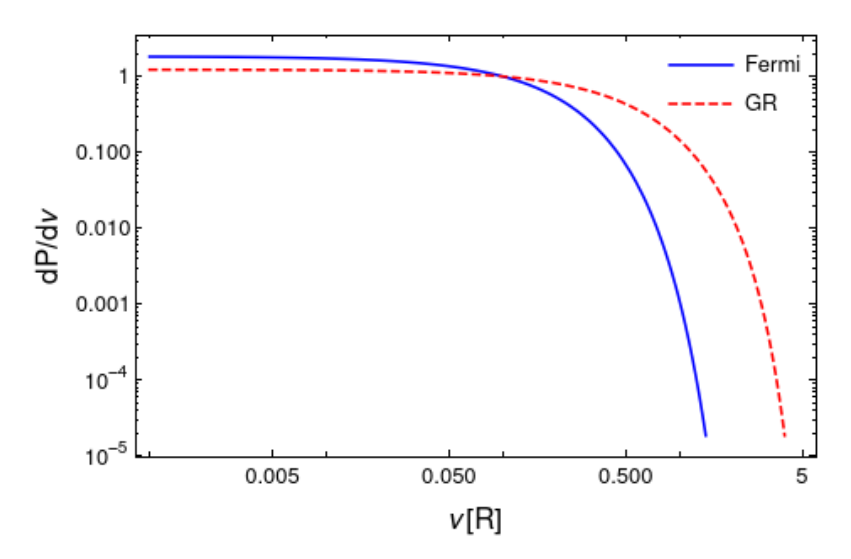


Figure 2.7: comparisons of the (normalized) value for the pressure gradient between Fermi and GR derivations. $\beta_0 = 0.1$; $\theta_0 = 0.2$

As one can see, the two curves do not coincide, which means that, for this specific model, the description of the galactic matter as fermi gas is not reconcilable with the derivation from GR. In other words, in the general case, the profiles violate energy-momentum conservation.

2.3 Brownsberger-Randall Model

The third model under consideration here, is the Brownsberger-Randall (BR) Model after its originators. First, we will rederive the model, as done by *Brownsberger et Randall* [28], and then analyse its limitations.

The BR-model is produces a dark matter and stellar probability density profile via maximum likelihood estimation, assuming

Dark matter, comprised out of a halo and a disk

- Halo: A parametrizable spheroidal dark matter density profile (including a cut-off radius); parametrized by the total mass, scale radius, ellipticity, polar axis orientations and spatial offset from the galactic center
- Disk: A hyperbolic, secant disk; parametrized by the total mass, scale radius, scale height, polar axis orientation and spatial offset from the galactic center
- Tracer: spheroidal symmetry; Isotropic and constant velocity dispersion; fixed angular velocity
- Binning such that the number of stars in each bin are Poisson distributed
- Availability of stellar positions (x, z) and velocity data $v_{LOS}(x, z)$.

2.3.1 Model

Contrary to the two previously introduced models, the BR-model considers both the galaxy's dark matter and tracer components.

Parametrizing halo and disk probability density

The total dark matter in the galaxy under consideration is modelled to be composed of a disk and a spheroidal halo. Three choices for the spheroidal dark matter halo density profile are given by *Brownsberger et Randall*. They are parametrized by a scale radius r_s , the total halo mass M_h and the ellipticity of the halo Q. For the halo mass to be finite, a cut-off c is introduced, where the density discontinuously

falls to 0 and cr_s is equal to the cosmological Virial radius $\left(\frac{M_h}{\frac{4\pi}{3}Q(cr_s)^3} = \Delta_c \rho_{crit,0}\right)$.

$$\rho_{halo} = \frac{M_h}{4\pi Q r_s^3} \begin{cases} \frac{1}{f(c)m'(1+m')^2} & (\text{NFW}) \\ \frac{1}{h(c)(1+m')^3} & (\text{Acored}) \\ \frac{1}{g(c)(1+m')(1+m'^2)} & (\text{Burkert}) \end{cases}$$
(2.43)

with

$$m'^{2} = \left(\frac{R}{r_{s}}\right)^{2} + \left(\frac{z}{r_{s}Q}\right)^{2}$$

$$f(c) = \ln(1+c) - \frac{c}{1+c}$$

$$h(c) = \ln(1+c) - \frac{2c+3c^{2}}{2(1+c)^{2}}$$

$$g(c) = \frac{1}{2}\left(\ln(1+c) + \arctan(c)\right)$$

where R refers to the radial distance and z to the height in cylindrical coordinates. The disk (consisting of baryons and dark matter) is modelled as a hyperbolic, secant disk in accordance with *Robin et alii* [29]:

$$\rho_{disk} = \frac{M_d}{8\pi R_d^2 z_d} \exp\left(-\frac{R}{R_d}\right) \operatorname{sech}\left(\frac{z}{2z_d}\right)$$
 (2.44)

which is parametrized by the total mass M_d , a scale radius R_d and scale height z_d .

Additional parameters are h_c and d_c , the vectorial halo and disk offset from the center respectively, and (ϕ,θ) and (b,a), the relative orientation of the halo and disk polar axes with respect to the observer's coordinate system respectively. Instead of M_d and M_h , disk and halo total mass, two new parameters are introduced: the total galactic mass M and ϵ , with $\epsilon = M_d/M$. Instead of z_d , the dimensionless parameter $\lambda = z_d/R_d$ is used. The parameter space is then defined by

$$\Theta = (M, r_s, Q, \phi, \theta, R_d, \epsilon, \lambda, b, a, h_c, d_c)$$
(2.45)

With fixed set of parameters Θ , ie knowledge of ρ_{halo} and ρ_{disk} , one can determine the potential via

$$\nabla^2 \Phi(x) = -4\pi G \rho(x) = -4\pi G (\rho_{halo}(x) + \rho_{disk}(x))$$
 (2.46)

Finding the stellar probability density

Like the dark matter particles, the galaxy's tracer components also obey Jean's equations. Since spheroidal symmetry was assumed for the stellar components, it is useful to employ the corresponding Jeans equations, as derived by *Binney et Tremaine* [11] (here, ρ^* will be treated as the tracer matter density - see footnote on page 15. The superscript * for the velocity moments is implied)

$$\frac{\partial \rho^* \overline{v_R}}{\partial t} + \frac{\partial \rho^* \overline{v_R^2}}{\partial R} + \frac{\partial \rho^* \overline{v_R v_z}}{\partial z} + \rho^* \left(\frac{\overline{v_R^2} - \overline{v_z^2}}{R} + \frac{\partial \Phi}{\partial R} \right) = 0$$
 (2.47)

$$\frac{\partial \rho^* \overline{v_z}}{\partial t} + \frac{\partial \rho^* \overline{v_R v_z}}{\partial R} + \frac{\partial \rho^* \overline{v_z^2}}{\partial z} + \frac{\rho^* \overline{v_R v_z}}{R} + \rho^* \frac{\partial \Phi}{\partial z} = 0$$
 (2.48)

The following assumptions are then made:

- the usual assumption of a static model $\frac{\partial f}{\partial t} = 0$
- isotropic velocity dispersion: $\sigma_{\phi}^2 = \sigma_{R}^2 = \sigma_{z}^2 = \sigma^2$
- constant velocity dispersion $\sigma^2(R) = \sigma^2$

- free streaming in ϕ -direction only: $v_R = v_z = 0$
- fixed angular velocity: $v_{\phi} = \omega R$

which simplifies the model:

$$\sigma^2 \frac{\partial \rho^*}{\partial R} - \rho^* \left(\omega^2 R - \frac{\partial \Phi}{\partial R} \right) = 0 \tag{2.49}$$

$$\sigma^2 \frac{\partial \rho^*}{\partial z} + \rho^* \frac{\partial \Phi}{\partial z} = 0 \tag{2.50}$$

This can be solved to yield a two-parameter density profile for stellar matter, which in addition also depends on the gravitational potential (which, in turn, is described by the gravitationally dominating dark matter component - see equation(2.46)):

$$\rho^*(R,z) = C \exp\left(\frac{\omega^2 R^2}{2\sigma^2} - \frac{\Phi(R,z)}{\sigma^2}\right)$$
 (2.51)

With a given expression for $\Phi(R,z)$, the parameters of the stellar model can be fixed with observational data (note that, for an isotropic system, $\sigma_{LOS}^2 = \sigma^2$), i.e. line-of-sight velocities and stellar position data. The velocity dispersion σ_A^2 and angular velocity ω_A^2 of population A.

$$\sigma_A^2 = \frac{1}{N_A} \sum_{n \in A} \left(\langle v_r' \rangle_A - v_{r,n}' \right)^2 \tag{2.52}$$

$$(\omega_A, w_{y,A}) = argmin_{p_1 \in R, p_0 \in R} \left(\sum_{n \in A} \frac{1}{\sigma_{v_{r,n}}^2} (v'_{r,n} - (p_1 R_n + p_0))^2 \right)$$
(2.53)

where p_1 and p_0 are fitting parameters and R_n is the distance of the nth star from the symmetry axis. w_y is the y-component of the star's proper motion and $v'_{r,n}$ represents the line of sight velocity of the nth star, with the effect of proper motion corrected for.

After finding the best-fit parameters, and with the form of the (dark matter dominated) gravitational potential known (Φ being parametrized by θ), one can calculate the projected stellar surface probability density $S(x_{sky}, z_{sky}, \Theta)$ (ρ^* is calculated as a set of finite points and thus $S(x_{sky}, z_{sky}, \Theta)$ is approximated using a Riemann sum) - see figure 2.8, for description of the coordinate system.

$$S(x_{sky}, z_{sky}, \Theta) = \int_{-D}^{\infty} \rho^*(x_{sky}, y_{sky}, z_{sky}, \Theta)$$
 (2.54)

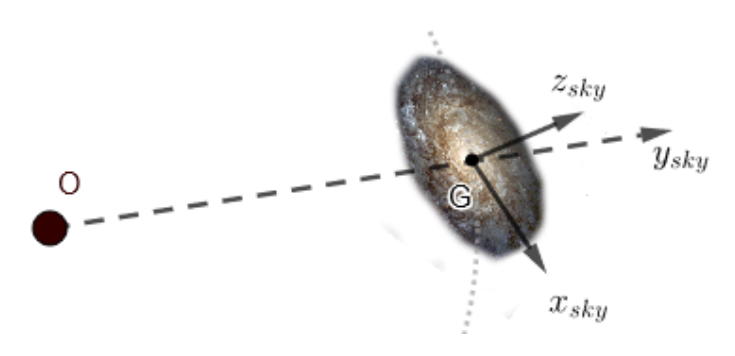


Figure 2.8: coordinate system under consideration. The background image of the NGC 4414 Galaxy was taken from [30]

Fitting probability density to data

Before, velocity measurements were used to fix the two parameters of ρ^* , now position data is used to constrain Φ (and thus also ρ^*). The probability to detect a star an position (x,z) is $O(x,z,\Theta)$, with

$$O(x,z,\Theta) = \frac{S(x,z,\Theta)D(x,z,\Theta)}{\int_{sky} dx'dz'S(x',z',\Theta)D(x',z',\Theta)}$$
(2.55)

where S(x,z) is the projected stellar surface probability density. D(x,z) is the probability that the observer O detects a star at position (x,z) and is calculated by considering the position dependent fraction of observed stars (i.e. those for which good v_{LOS} were measured) to candidate stars. In the following, the three DM halo models are considered separately and the best fit parameters for each found. After this one can compare the best fit profiles for NFW, Acored and Burkert and determine which of these fit the data the best.

The sky area of the galaxy (containing N_* stars) is divided into N bins of area A. The probability, for an assumed stellar distribution $O(x, z, \Theta)$, of observing a number n_i of stars in bin i is assumed to follow a Poisson distribution

$$\mathcal{L}_{i}(n_{i}|O(\Theta), N_{*}) = \frac{e^{-N_{*,i}}(N_{*,i})^{n_{i}}}{n_{i}!}$$
(2.56)

$$N_{*,i} = N_* \int_{bini} dx' dz' O(x', z', \Theta)$$

$$\sim N_* O(x_i, z_i, \Theta) A$$
(2.57)

If the bin size is reduced enough until every bin contains either 0 or 1 star, then the combined likelihood over all observed stars is

$$\mathcal{L}(n|O(\Theta), N_*) = \prod_{i=1}^{N} \mathcal{L}(n_i|O(\Theta), N_*)$$

$$= e^{-N_*} (N_* A)^{N_*} \prod_{(x_*, z_*)} O(x_*, z_*, \Theta)$$
(2.58)

with (x_*, z_*) representing the sky coordinates of the stars. The relative likelihood gives a measure for the relative fit quality of a model/parameter set $O_{\theta 1}$ with respect to a model/parameter set $O_{\theta 2}$.

$$r_{12} = \frac{\mathcal{L}_1}{\mathcal{L}_2} = \frac{\prod_{(x_*, z_*)} O_{\theta 1}(x_*, z_*)}{\prod_{(x_*, z_*)} O_{\theta 2}(x_*, z_*)}$$
(2.59)

Using bootstrapping set, i.e. randomly selecting N_* stars out of the original data set with replacement, one can repeat this analysis for these artificial galaxies and can thus determine the robustness of the measure r_{12} . After choice of a DM model, a Markov Chain Monte Carlo (MCMC) is used to find the best fit parameters via a series of random walks through the parameter space. After each step the likelihood ratio r_{12} between old and new points is determined and compared to a random number between 0 and 1. The new point is rejected if the ratio is smaller than the random number. This analysis is repeated six times: for each of the three models, with and without a disk.

Results

We will, in the following, cite the results of the fitting algorithm, i.e. list the values *Brownsberger et Randall* recover as best-fit parameters.

Figure (2.9) lists those best-fit parameters for various dark matter density profiles, all of them considering a dark matter mass distribution found in both halo and disk $\rho_{DM} = \rho_{halo} + \rho_{disk}$. As suggested by the non-zero best-fit value of ϵ , placing a small amount of matter in the disk improves the fit. Nevertheless, the value for ϵ is very small, leading to the parameters associated with the disk to have little impact on the overall fit quality. The value for the total galactic mass M converges to the outer region of the parameter space, suggesting that the true best-fit parameter for M is larger than allowed by the MCMC algorithm upper-limit for M. The fit-results for the halo without disk suggest that the halo is cored, as the Acored profile is always a better fit than the NFW profile. There also seems to be a preference for the Acored profile over the Burkert profile. [28]

2.3.2 Validity

Similarly to the RSU-Model, the main limitations of Brownsberger-Randall model lies in its narrow assumptions. The stellar velocity dispersion is not only thought to be isotropic, but constant with radius (which is more limiting than the assumption made for the RSU-model). Besides this, the angular velocity of the tracer is also fixed to be constant. It's main improvement over other attempts at fitting density profiles to velocity data, is the idea that some of the dark matter content might be found in a disk and a spheroidal halo, rather than in a spherical halo alone. However, while the parameter ϵ describing the amount of matter situated in the halo is non-zero, the existence of a disk does not greatly improve the fit quality in general.

Halo Type	M	r_s	Q	θ	ψ	$\mathbf{h}_c \; (\mathrm{pc}, \mathrm{pc}, \mathrm{pc})$	$\ln \tilde{\mathcal{L}}$
_	ϵ	R_d (pc)	λ	a	\boldsymbol{b}	\mathbf{d}_c (pc, pc, pc)	_
NFW; oblate	9700 ± 1600	7100 ± 1600	0.427^{*}	134.1*	0*	$(-77 \pm 28, 0^*, -138 \pm 28)$	21421.8
	$0.030^{+0.203}_{-0.019}$	6000 ± 1300	0.1^{*}	178*	0*	$(-6.0 \pm 670, 0^*, -370 \pm 420)$	
NFW; prolate	9700 ± 1600	3900 ± 1300	2.16*	44.2^{*}	0*	$(-76 \pm 29, 0^*, -137 \pm 26)$	21421.6
_	$0.039^{+0.143}_{-0.024}$	6000 ± 1300	0.1^{*}	178*	0*	$(-80 \pm 250, 0^*, -350 \pm 300)$	
Acored; oblate	3600 ± 1000	1900 ± 320	0.466*	133.7^{*}	0*	$(-73 \pm 17, 0^*, -144 \pm 16)$	21430.0
_	$0^{+0.14}_{-0}$	6800 ± 1100	0.1^{*}	178*	0*	$(-120 \pm 70, 0^*, 220 \pm 410)$	
Acored; prolate	2870 ± 880	1000 ± 170	2.04^{*r}	43.8*	0*	$(-74 \pm 17, 0^*, -146 \pm 16)$	21424.9
	$0^{+0.14}_{-0}$	1290 ± 260	0.1^{*}	178*	0*	$(-86 \pm 24, 0^*, -150 \pm 14)$	
Burkert; oblate	390 ± 770	1290 ± 260	0.466*	133.7^{*}	0*	$(-73\pm16,0^*,-147\pm16)$	21428.6
_	$0.0041^{+0.0028}_{-0.0013}$	8100 ± 2200	0.1^{*}	178*	0*	$(-180 \pm 280, 0^*,^{\ddagger})$	
Burkert; prolate	520 ± 370	840 ± 130	2.02*	43.9*	0*	$(-72\pm18,0^*,-145\pm15)$	21428.4
	$0.0040^{+0.0036}_{-0.0013}$	8300 ± 1700	0.1^{*}	178*	0*	$(-170 \pm 23, 0^*, -140 \pm 78)$	

Figure 2.9: Best fit parameters for various dark matter density profiles, all of them including both a halo and a disk. Taken from [28]

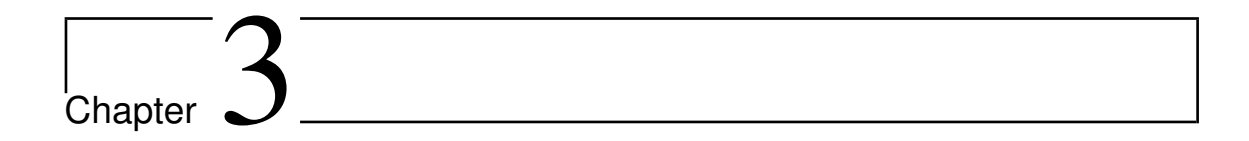
Looking at the values for the log-likelihood in figure (2.9), initially casts doubt on the validity of the best-fit parameters (for a good fit, L over the number of categories k $L/k \sim 1$). However, the situation might be easily remedied: With a typical value of e^{21421} for the renormalized likelihood $\overline{\mathcal{L}}$, we have, for \mathcal{L} :

$$\mathcal{L} = e^{-N_*} (N_* A)^{N_*} \prod_{(x_*, z_*)} O(x_*, z_*, \Theta)$$
 (2.60)

$$\mathcal{L} = e^{-N_*} (N_* A)^{N_*} \prod_{(x_*, z_*)} O(x_*, z_*, \Theta)$$

$$\overline{\mathcal{L}} = \prod_{(x_*, z_*)} O(x_*, z_*, \Theta) = e^{21421} \to \mathcal{L} = e^{21421 - N_*} (N_* A)^{N_*}$$
(2.61)

With $N_* = 2498$, we can estimate A, the area of the bin, using two extreme cases: In this way, the value for A is found to lie between $1.5996 * 10^{-11} pc^2$ (projected area for a typical RG star) and $142.659pc^2$ (total projected area of the galaxy divided by the number of stars). With these estimates, the likelihood L divided by the number of categories k gives a value between $6.412 * 10^{-16}$ and 96.322, which includes the ideal case of $L/k \sim 1$. Specifically, for an area of 1.55397 pc^2 we have $L/k \sim 1$.



Lower mass bound with parametrized dark matter models

We will now derive lower mass bounds for fermionic dark matter particles in LG dwarf Spheroidals based on the Tremaine-Gunn bound and a simple fitting procedure. Similar to the approach of *Brownsberger et Randall*, the following models assume a parametrized dark matter density profile and fit it to observational data.

In both cases, the dark matter profile assumes some expression, which is well-motivated by previous literature in the field. *Brownsberger et Randall* [28] choose a stellar density profile which is a solution to the spheroidal, isotropic Jeans equations. The thereby constructed set of parameters predicts values for line-of-sight velocities, angular velocities, and projected number densities. These can be used to find the best-fit set of parameters. *Richardson et Fairbairn* [15], as well as *Read et Steger* [14], choose parametrized stellar density and anisotropy profiles, which predict values for line-of-sight velocities and Virial shape parameters (i.e. higher order line-of-sight velocity moments).

3.1 Richardson-Fairbairn profiles

The Richardson-Fairbairn (RF) model [15], yields a dark matter profile (set to describe the Sculptor dSph) based on maximum likelihood estimation and using Virial shape parameters, assuming

- spherical symmetry
- a parametrizable expression for dark matter density profile $\rho_{DM}(r)$ (e.g. Zhao parametrization), stellar density profile $\rho^*(r)$ (here: one parameter Plummer profile) and stellar anisotropy parameter $\beta(r)$ (e.g. constant)
- a set of line-f-sight velocity measurements $v_{z,i}$ (moments of the stellar velocity distribution) and projected radii R_i

Virial shape parameters

For this approach, one refers to the definition of the Virial equations, as defined in section (1.2.4) (The superscript *, denoting affinity to the stellar distribution, for the velocity moments, for the projected density Σ , and for the anisotropy parameter is implied):

$$3\int_0^\infty \Sigma(R)\overline{v_{LOS}^2(R)}RdR = 2\int_0^\infty \rho^* \frac{d\Phi(r)}{dr}r^3dr \tag{3.1}$$

$$\int_0^\infty \Sigma \overline{v_{LOS}^4} R dR = 2 \int_0^\infty \rho^* \overline{v_r^2} \left(1 - \frac{2}{5} \beta \right) \frac{d\Phi}{dr} r^3 dr \tag{3.2}$$

$$\int_0^\infty \Sigma \overline{v_{LOS}^4} R^3 dR = 2 \int_0^\infty \rho^* \overline{v_r^2} \left(1 - \frac{6}{7} \beta \right) \frac{d\Phi}{dr} r^5 dr \tag{3.3}$$

The left-hand-sides are associated with weighted averages (over the entire radial space) for the quantities $\overline{v_{LOS}^2}$, $\overline{v_{LOS}^4}$ and $\overline{v_{LOS}^4}R^2$ (denoted by brackets $\langle \rangle$ in the following)

This lets us construct the Virial shape parameters:

$$\zeta_A = \frac{\langle \overline{v_z^4} \rangle}{\langle \overline{v_z^2} \rangle^2} = \frac{9N_{tot}}{10} \frac{\int_0^\infty \rho^* (5 - 2\beta) \overline{v_r^2} \frac{d\Phi}{dr} r^3 dr}{(\int \rho^* \frac{\partial \Phi}{\partial r} r^3 dr)^2}$$
(3.4)

$$\zeta_B = \frac{\langle \overline{v_z^4} R^2 \rangle}{\langle \overline{v_z^2} \rangle \langle R^2 \rangle} = \frac{9N_{tot}^2}{35} \frac{\int_0^\infty \rho^* (7 - 6\beta) \overline{v_r^2} \frac{d\Phi}{dr} r^5}{(\int \rho^* \frac{\partial \Phi}{\partial r} r^3 dr)^2 \int \Sigma R^3 dR}$$
(3.5)

Upon knowledge of the theoretical parameters governing density profiles and anisotropy parameter, the right-hand-side of these equations can be reconstructed easily. The expression on the left-hand-side is used to derive the shape parameter from data. One differentiates between "true" (i.e. derived from theoretical parameters) shape parameters $\hat{\zeta}$ and those derived from data $\hat{\zeta}$.

$$\hat{\zeta}_A = N_s \frac{\sum_i^{N_s} v_{z,i}^4}{(\sum_i^{N_s} v_{z,i}^2)^2}$$
(3.6)

$$\hat{\zeta}_B = N_s^2 \frac{\sum_i^{N_s} v_{z,i}^4 R_i^2}{(\sum_i^{N_s} v_{z,i}^2)^2 \sum_i^{N_s} R_i^2}$$
(3.7)

Experimental errors introduce a bias between predicted and measured shape parameters, $\hat{\zeta} - \zeta$. *Richardson et Fairbairn* attempt to reconstruct this bias from simulated data provided by the Gaia challenge test data set (here for a galaxy the same size as Sculptor) [31]. For various parameter sets, this relation is obtained by fitting a power law to the $\hat{\zeta}(\zeta)$ curve (see figure 3.1).

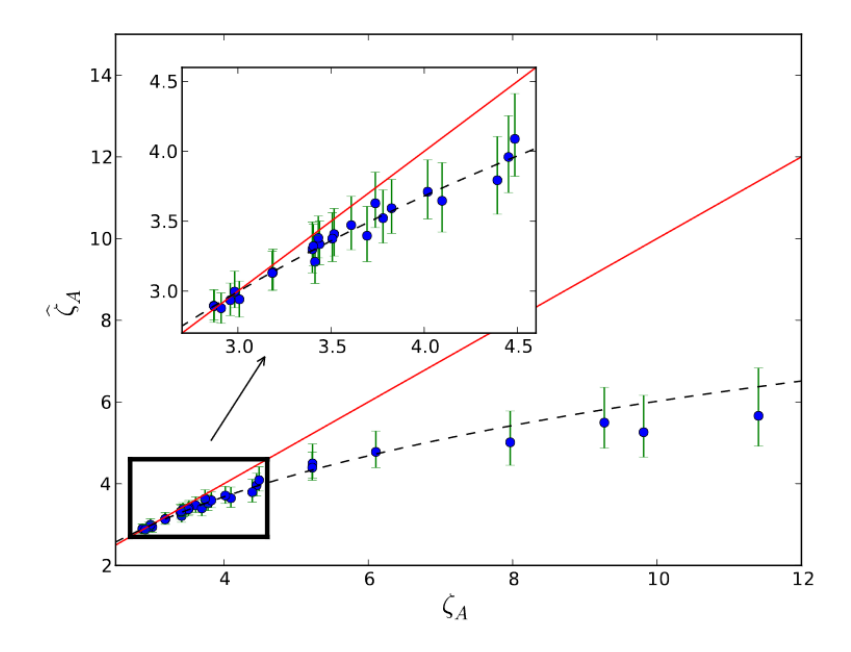


Figure 3.1: Data points for biased (i.e. inferred from observation) $\hat{\zeta}$ and unbiased ζ shape parameter estimators as inferred from the Gaia challenge test data. Different values for ζ correspond to differences in the underlying parameter set. The red line corresponds to a truly unbiased estimator, the dashed line to the power law. This image was taken from [15]

Standard Jeans analysis + Virial estimators

The method, following Richardson et Fairbairn, builds upon a standard Jeans analysis, i.e. a maximum likelihood estimation effectuated by fitting parametrized density and anisotropy profiles to line-of-sight velocity data aided by Jeans-equations. The analysis involves steps of different methodology.

 Analytical To perform the fit, parametrizable models for stellar density, DM density and stellar anisotropy parameter are chosen:

$$\rho^*(r) = \frac{\rho_0^*}{\left(\frac{r}{r^*}\right)^{\gamma^*} \left[1 + \left(\frac{r}{r^*}\right)^{\alpha^*}\right]^{(\beta^* - \gamma^*)/\alpha^*}} \tag{3.8}$$

$$\rho^*(r) = \frac{\rho_0^*}{\left(\frac{r}{r^*}\right)^{\gamma^*} \left[1 + \left(\frac{r}{r^*}\right)^{\alpha^*}\right]^{(\beta^* - \gamma^*)/\alpha^*}}$$

$$\rho_{DM}(r) = \frac{\rho_0}{\left(\frac{r}{r_d}\right)^{\gamma_d} \left[1 + \left(\frac{r}{r_d}\right)^{\alpha_d}\right]^{(\beta_d - \gamma_d)/\alpha_d}}$$
(3.8)

$$\beta(r) = (\beta_{\infty} - \beta_0) \frac{r^2}{r_{\beta}^2 + r^2} + \beta_0 \tag{3.10}$$

The density models are termed Zhao profiles, the anisotropy parameter is restricted such that it decreases/increases monotonically between β_0 and β_{∞} . Upon choice of a set of parameters p, we can infer the radial velocity dispersion from the stellar Jeans equation (again, the superscript * for the velocity moments, the projected density Σ , and the anisotropy parameter is implied)

$$\frac{\partial}{\partial r}(\overline{v_r^2}\rho^*) + \frac{2}{r}\rho^*\overline{v_r^2}\beta = -\rho^*\frac{\partial\Phi}{\partial r}$$
(3.11)

which in turn lets us predict a value for the line-of-sight velocity dispersion (see equation (1.34)):

$$\Sigma(R)\overline{v_{LOS}^2(R)} = 2\int_R^\infty \left(1 - \beta(r)\frac{R^2}{r^2}\right) \frac{\rho^*(r)\overline{v_r^2(r)}r}{\sqrt{r^2 - R^2}} dr \tag{3.12}$$

and projected 2D mass density (due to Merrifield et Kent [17])

$$\Sigma(R) = 2 \int_{R}^{\infty} \rho^{*}(r) \frac{rdr}{\sqrt{r^{2} - R^{2}}}$$
 (3.13)

- From data A data set of projected radii and line-of-sight velocities $d = (R_i, v_{z,i})$ is needed. The variance of $v_{z,i}$ at fixed radii is then used as the measured dispersion $S_{2,i}$
- From simulations Using the chosen parameters, data is simulated and analysed via bootstrapping. This allows us to obtain values for the variance of the velocity dispersion $Var[S_{2,j}]$ and, similarly to the process described in the previous subchapter, a bias on the mean of the $S_{2,i}$ distribution: $b_i = Mean[S_{2,i}] \overline{v_z^2}(R_i|p)$

All of these steps allow for the likelihood value to be calculated via

$$\mathcal{L}(d|p) = \prod_{j}^{N_b} \frac{1}{\sqrt{2\pi Var[S_{2,j}]}} \exp\left(-\frac{[S_{2,j} - \overline{v_z^2}(R_j|p) - b_j]^2}{2Var[S_{2,j}]}\right)$$
(3.14)

The new approach due to *Richardson et Fairbairn* is now to include information on the Virial shape parameters as a consistency check and to further constrain the model. With the measured data, one can construct the Virial shape parameters, using expressions (3.6) and (3.7). Since one has a set of presumed parameters p, one can also calculate these parameters, purely from theory, using expressions (3.4) and (3.5). Taking the bias that was inferred from simulations into account, one can compare the Virial shape parameters from data and from parameters and thus obtains an independent constraint that can be used to break mass-anisotropy degeneracy

Results

Richardson et Fairbairn apply their analysis to the Sculptor dSph, with data published by Walker et alii [32]. In the first instance, the velocity anisotropy was chosen to be constant, the stellar density to follow a simple Plummer profile and the dark matter density profile to either take the form of a Burkert or NFW profile:

$$\rho_{DM,Burkert}(r) = \frac{\rho_0 r_s^3}{(r_s + r)(r_s^2 + r^2)}$$

$$\rho_{DM,NFW}(r) = \frac{\rho_0 r_s^3}{r(r^2 + r_s^2)}$$
(3.15)

$$\rho_{DM,NFW}(r) = \frac{\rho_0 r_s^3}{r(r^2 + r_s^2)}$$
 (3.16)

Then r_s , β , and ρ_0 are varied to find the best fit to the data. The median, 1σ , and 2σ confidence intervals, resulting from a fit of (restricted to be constant) anisotropy parameter to line-of-sight velocity data are displayed in figure (3.2) (blue regions).

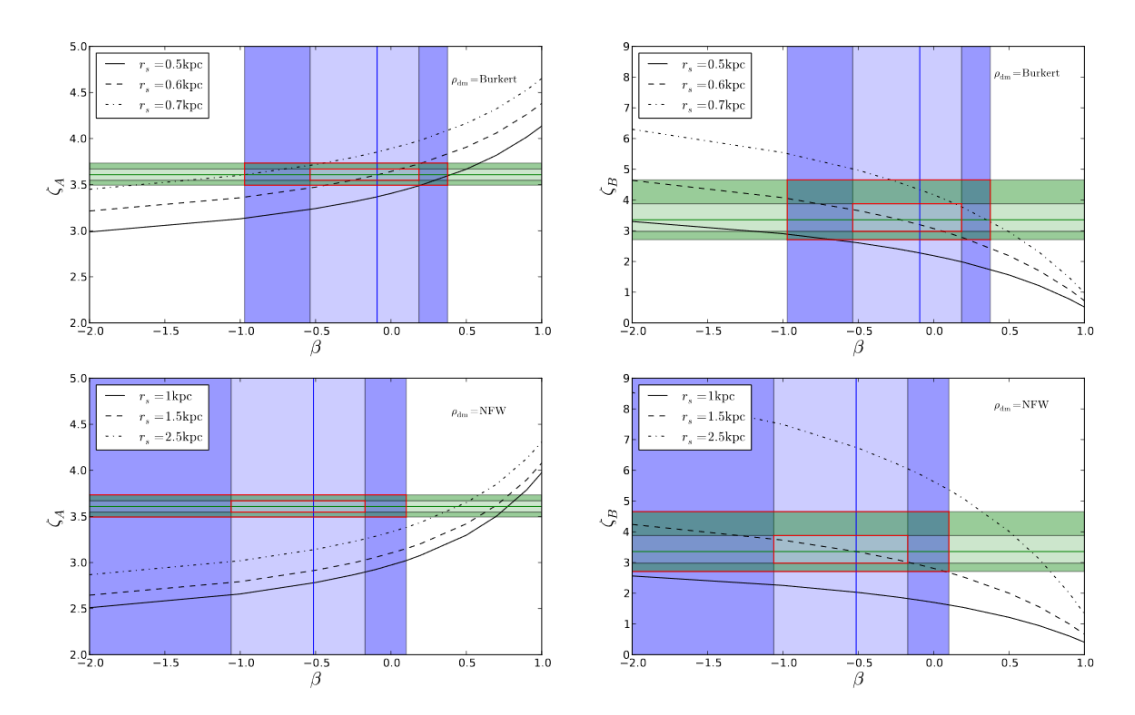


Figure 3.2: Results of Jeans analysis+Virial shape parameters for Sculptor with constant anisotropy profile. The top row of plots gives results for the Burkert profile, the bottom row results for the NFW profile. The first (second) column plots Virial shape parameter ζ_A (ζ_B) vs the - restricted to be constant - stellar anisotropy parameter β . The green shaded regions describe the measured (and bias corrected) Virial Shape parameters. The blue shaded regions describe β as inferred from LOS data. The black lines give the result of the remaining free parameter, scale radius r_s , on the theoretical Virial shape parameter. Taken from [15]

From data, we can also infer the measured Virial shape parameters to be $\zeta_A' = 3.43$ and $\zeta_B' = 3.69$ (this is without the correction via the bias from simulations. The green regions in figure (3.2) represent the bias corrected Virial shape parameters). ζ'_A and ζ'_B are, therefore, derived purely from data, without explicitly varying and fitting any parameters. The Virial shape parameters are useful in this case, since they are normalized to be independent of ρ_0 , reducing the number of degrees of freedom and leaving only the scale radius r_s and anisotropy parameter β as free parameters. With β fixed from LOS-data, the black lines in the following graph show the effect of scale radius on the theoretical ζ_A and ζ_B . For the parametrization to make sense for Sculptor, they should pass through the red squares.

For the next step, the same Plummer and NFW/Burkert profiles (free parameters: scale radius and core density) were chosen by *Richardson et Fairbairn* for the tracer and DM distribution respectively. However, the velocity anisotropy parameter now follows equation (3.10). By varying the five different parameters, they obtain a range of χ^2 values that are plotted against the core radius (see figure (3.3)).

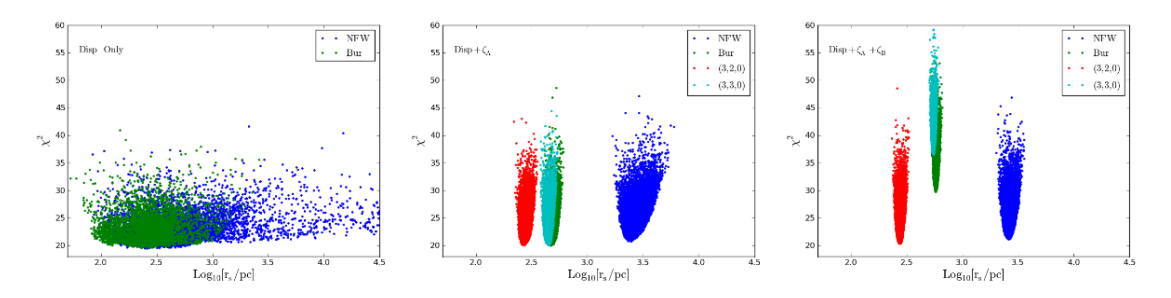


Figure 3.3: χ^2 vs r_s plots, representing the fit result with non-constant anisotropy parameter. In the first panel, only the dispersion data was used for the fit, in the second panel ζ_A was added to the analysis and finally, dispersion + ζ_A + ζ_B data were used in the third panel. The different colors refer to different dark matter density profiles. Taken from [15]

The best fit for the scale radius narrows down, as we begin to include Virial shape parameters. The left-most panel of figure (3.3) is a typical example for the $\rho-\beta$ -degeneracy problem: Without Virial shape parameters, both NFW (blue dots) and Burkert (green dots) profile deliver good fit results to dispersion data alone. The right-most panel shows that inclusion of both Virial shape parameters enables distinction between the two density profiles, with the NFW being a better fit than the Burkert profile (see [15]). This suggests that the $\rho-\beta$ -degeneracy can be broken with Virial shape parameters.

3.1.1 Comparison to Read-Steger profiles

Before calculating the mass bounds for these profiles, we will first discuss the slight differences between the method of *Richardson et Fairbairn* and the Read-Steger (RS) profile [14]. As can be inferred in table (3.1), the main difference in the two approaches lies in the description of the bias and the definition of the Virial estimators. Figure (3.4) shows the difference in performance of the two

methods. The closer the data points are to the dashed line (true VSP) the more accurate the estimator. [14]

As can be inferred, the higher the number of simulated stars, the more accurate the estimator. However, for cusped profiles and the second Virial estimator, there is a significant difference between the true Virial shape parameters and those derived by either method. This holds true, even for a high number of simulated stars. We assume that these errors are related to a comparatively poor data reconstruction quality at larger radii specifically. This is because cusped profiles and the second Virial shape parameter (goes as a sum over $\overline{v_z^4}R^2$ as opposed the first Virial shape parameter, which goes as a sum over $\overline{v_z^4}$) are expected to be more sensitive to data at larger radii.

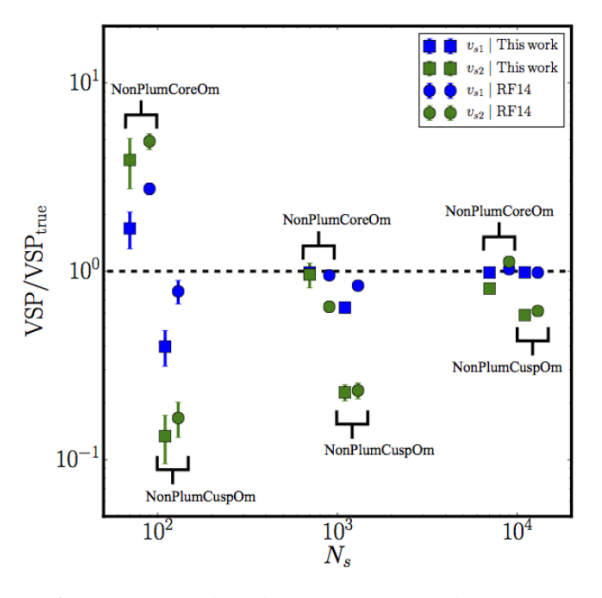


Figure 3.4: VSP/VSP_{true} for RF (circular data points) and RS (square data points) models for two Gaia Challenge mock data sets (NonPlumCoreOm and NonPlumCuspOm). The blue (green) data points refer to the performance of the first (second) Virial estimator. There is a small vertical offset for discernibility. Taken from [14]

Richardson et Fairbairn

Read et Steger

Zhao density profiles
$$\rho^*(r) = \frac{\rho_0^*}{\left(\frac{r}{r^*}\right)^{\gamma^*}\left[1+\left(\frac{r}{r^*}\right)^{\alpha^*}\right]^{\frac{\beta^*-\gamma^*}{\alpha^*}}} \\ \rho_{DM}(r) = \frac{\rho_0}{\left(\frac{r}{r^*}\right)^{\gamma^*}\left[1+\left(\frac{r}{r^*}\right)^{\alpha}\right]^{\frac{\beta^*-\gamma^*}{\alpha^*}}} \\ \rho_{DM}(r) = \frac{\left(\frac{r}{r_d}\right)^{\gamma_d}\left[1+\left(\frac{r}{r_d}\right)^{\alpha_d}\right]^{\frac{\beta_d-\gamma_d}{\alpha_d}}}{\left(\frac{r}{r_d}\right)^{\gamma_d}\left[1+\left(\frac{r}{r_d}\right)^{\alpha_d}\right]^{\frac{\beta_d-\gamma_d}{\alpha_d}}} \\ \rho_{DM}(r) = \begin{cases} \rho_0\left(\frac{r}{r_0}\right)^{-\gamma_0} \\ \rho_0\prod_{n=0}^{j< N_{dm}}\left(\frac{r_{n+1}}{r_n}\right)^{-\gamma_n}\left(\frac{r}{r_{j+1}}\right)^{\gamma_j+1} \end{cases} \\ \rho_0(r) = \left(\frac{r}{r_0}\right)^{\frac{\gamma_d}{\gamma_d}} \\ \rho_0(r) = \left(\frac{r}{r_0}\right)^{\frac{\gamma_d}{\gamma_$$

The underlying method is based on a standard Jeans analysis in both cases. The parametrized profiles are used to predict line-ofsight velocities and Virial estimators (see below).

Virial shape parameters
$$\zeta_A = \frac{9N_{tot}}{10} \frac{\int_0^\infty \rho^*(5-2\beta)\overline{v_r^2} \frac{d\Phi}{dr} r^3 dr}{(\int \rho^* \frac{\partial\Phi}{\partial r} r^3 dr)^2}$$

$$= N_s \frac{\sum_{i}^{N_s} v_{z,i}^2}{(\sum_{i}^{N_s} v_{z,i}^2)^2}$$

$$\zeta_{B} = \frac{9N_{tot}^{2}}{35} \frac{\int_{0}^{\infty} \rho^{*}(7-6\beta)\overline{v_{r}^{2}} \frac{d\Phi}{dr} r^{5}}{(\int \rho^{*} \frac{\partial\Phi}{\partial r} r^{3} dr)^{2} \int \Sigma R^{3} dR}$$
$$= N_{s}^{2} \frac{\sum_{i}^{N_{s}} v_{z,i}^{4} R_{i}^{2}}{(\sum_{i}^{N_{s}} v_{z,i}^{2})^{2} \sum_{i}^{N_{s}} R_{i}^{2}}$$

Velocity moments $v_{s1} = \frac{2}{5} \int_0^\infty \rho^* (5 - 2\beta) \overline{v_r^2} \frac{d\Phi}{dr} r^3 dr$ $= \int_0^\infty \Sigma \overline{v_z^4} R dR$

$$\begin{array}{l} v_{s2} = \frac{4}{35} \int_{0}^{\infty} \rho^{*} (7 - 6\beta) \overline{v_{r}^{2}} \frac{d\Phi}{dr} r^{5} dr \\ = \int_{0}^{\infty} \Sigma v_{z}^{4} R^{3} dR \end{array}$$

Note that the Virial shape parameters sum over the observational data points to obtain the averages, whereas the velocity moments integrate over the data points (requiring an interpolation curve to the data points) to do the same

The quantities $\hat{\zeta}_A$ and $\hat{\zeta}_B$ are calculated from $\overline{v_z^2}$ and $\overline{v_z^4}$ data (equations (3.6) and (3.7)) using summation. After choice of a parametrizable model, one can calculate ζ_A and ζ_B (equations (3.4) and (3.5)). With the same choice of parameters, one simulates galaxies with the same ζ_A and ζ_B . The measured values $\hat{\zeta}_{A,sim}$ and $\hat{\zeta}_{B,sim}$ are used to infer the bias $\hat{\zeta}_{A,sim} - \zeta_A$ and $\zeta_{B,sim} - \zeta_B$. The bias is then fit with a power law such that one obtains the relations $\hat{\zeta}_{A,sim}(\zeta_A) \approx$ $\hat{\zeta}_A(\zeta_A)$ and $\hat{\zeta}_{B,sim}(\zeta_B) \approx \hat{\zeta}_B(\zeta_B)$ (see figure (3.1)) which, for the actual observation, are considered when fitting the values ζ_A and ζ_B

The quantities v_{s1} and v_{s2} are directly calculated from $\overline{v_z^4}$ data (eq (3.2) and (3.3), lhs) using numerical integration over Σ . Errors on v_{s1} and v_{s2} are directly considered via Monte Carlo sampling, by adding errors from simulations to the v_{τ}^4 data in order to obtain v_{s1*} and v_{s2*} After choice of a parametrizable model, one can calculate v_{s1} and v_{s2} (eq (3.2) and (3.3) rhs). The fit is realised with v_{s1*} and v_{s2*} (i.e. the errors already accounted for) and v_{s1} and v_{s2}

Table 3.1: Comparison of methods by Richardson et Fairbairn and Read et Steger

to $\hat{\zeta}_A$ and $\hat{\zeta}_B$.

3.2 Mass bounds 49

3.2 Mass bounds

With data generated from the Read-Steger model (see figures (3.5) and (B.1)), one can calculate lower mass bounds for the dark matter particle using the Tremaine-Gunn bound outlined in section (1.1). We approximate the phase-space density via coarse graining as described in section (1.1):

$$\overline{F}_{DM} = \frac{\rho(r)}{m_{DM}V(r)_{ms}} \tag{3.17}$$

with $V(r)_{ms}$ as the volume in momentum space (approximated by $\frac{4}{3}\pi p_{max}^3 = \frac{4}{3}\pi m_{DM}^3 v_{esc}^3$), one obtains the lower mass bound for a dark matter particle as a consequence of the Tremaine-Gunn bound:

$$m_{DM} \ge \left(\frac{\hbar^3 6\pi^2 \rho(r)}{g v_{esc}^3(r)}\right)^{1/4} \tag{3.18}$$

3.2.1 Profiles

The density and mass profiles constructed from data from the Read-Steger profiles (see figure (3.5) and (3.6) extend only to a radius of about 1.5 kpc. Not considering the enclosed mass past this radius R_{edge} might lead to significant underestimation of the escape velocity. For this reason, we elect to extend the density and mass profiles via extrapolation.

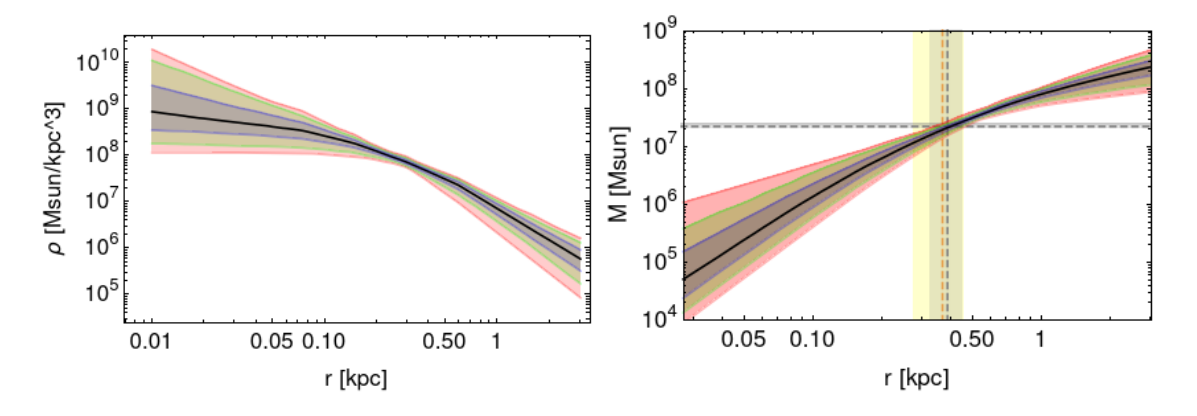


Figure 3.5: (left) LeoI dark matter density profile, (right) LeoI dark matter mass profile from data provided by Read et alii with (68%, 95% and 99%) confidence intervals. For the mass profile, the shaded regions signify the 3D half-light radius and half-light radius enclosed mass as reported by Wolf et alii [10]. The yellow shaded region marks the region of lowest relative error in the mass profile, which, following the theory of Wolf et alii should enclose the half-light radius. This is clearly the case here

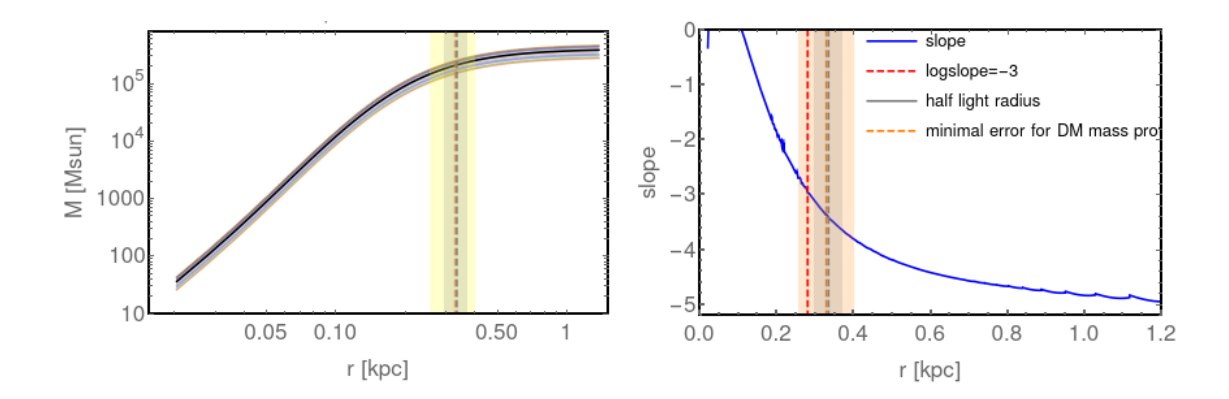


Figure 3.6: (left) stellar mass profile of the Carina dSph. Like in figure 3.5, the yellow shaded region marks the region of lowest relative error in the mass profile and the gray region the region containing the half light radius. (right) log-log slope of the density profile for the Carina dSph from data provided by Read et alii. The point where the slope yields -3 is marked by the dashed red line. According to the theory of Wolf et alii [10], this radius should be close to the half-light radius (gray dashed line within gray region) which itself should lie within the region of minimal error for the dark matter density profile (orange dashed line within orange region). Clearly, the data aligns with what the theory demands of stellar and density profiles

The extension of the profiles is effectuated as follows. Based on figure (3.10) for the log-log slopes associated with the dark matter density and enclosed mass, we can infer that the slopes approach a constant value at outer radii. This constant value is approximated by taking the average value of the slope between 0.9 R_{edge} (red line) and R_{edge} . This is done for both median profiles and confidence intervals. The profiles are then extended simply by extrapolating this approximately constant log-log slope up until a new R_{edge} of our choosing.

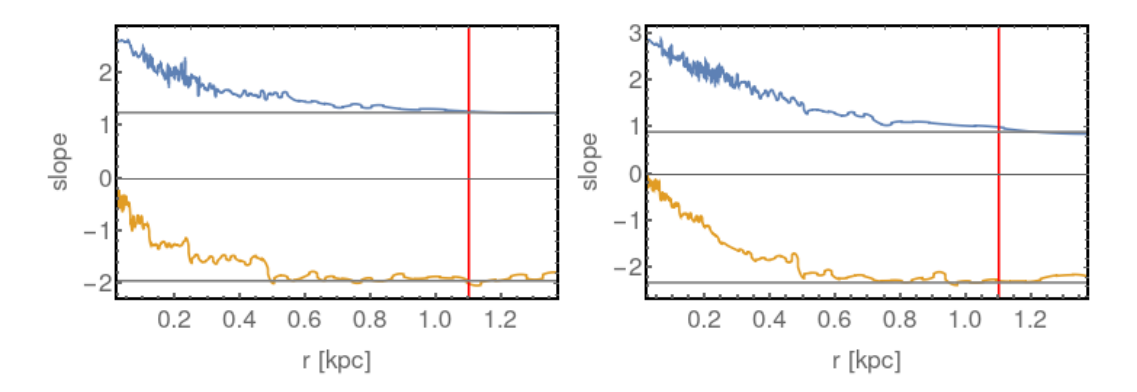


Figure 3.7: (left) median log-log slope (right) 68% low log-log slope for Carina. The mass profile is given in blue, whereas the density profile is given in orange. As an example, the median log-log slope of the mass profile approaches a constant value of 1.244

To achieve a sufficiently broad range for the profiles, one choice of R_{edge} is the Virial radius, which depends on the dark matter density profile via:

3.2 Mass bounds 51

$$\rho(r_{vir}) = \Delta_c \rho_c = \Delta_c \frac{3H(t)^2}{8\pi G} \sim 200 \cdot 136.4599 \tag{3.19}$$

Another is to extend the radius up until 100kpc, which leads to a very conservative estimate of the escape velocity, as this is more than the typical separation between most LG dSphs. In the following, all three choices for R_{edge} will be considered: a) the original radius of about 1.5kpc without any extrapolation, b) extrapolation up until the Virial radius, and c) extrapolation up until 100 kpc.

3.2.2 Bounds

The squared escape velocity $v_{esc}^2(r)$ (see figure (3.8)) becomes:

$$v_{esc}^{2}(r) = 2G \int_{r}^{R_{edge}} \frac{M(r')}{r'^{2}} dr' + \frac{2GM(R_{edge})}{R_{edge}}$$
(3.20)

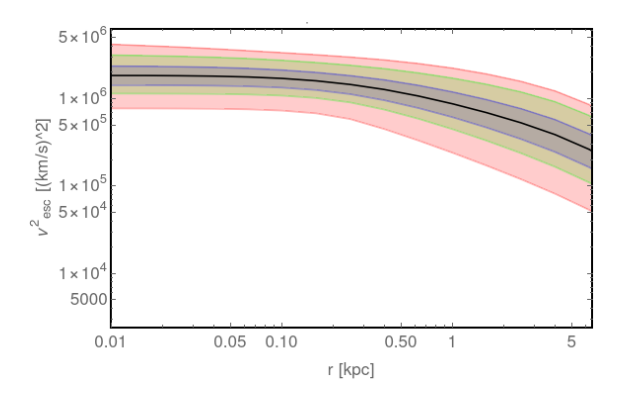


Figure 3.8: LeoII escape velocities with data provided by Read et alii

The squared escape velocity is linear in the mass data. Since the errors at different radii have to be assumed to be correlated, we impose conservative error estimates:

$$\sigma_{v_{esc}^2}(r) = 2G \int_r^{R_{edge}} \frac{\sigma_{M(r')}}{r'^2} dr' + \frac{2G\sigma_{M(R_{fin})}}{R_{edge}}$$
(3.21)

Where σ stands for the confidence interval width at the chosen confidence level and for the respective variable. For e.g. the 95% confidence interval in $v_{esc}^2(r)$ (i.e. $[v_{esc}^2(r) - \sigma_{v_{esc}^2,95low}(r), v_{esc}^2(r) + \sigma_{v_{esc}^2,95high}(r))$, we have:

$$\sigma_{v_{esc}^{2},95high}(r) = 2G \int_{r}^{R_{edge}} \frac{\sigma_{M(r'),95high}}{r'^{2}} dr' + \frac{2G \cdot \sigma_{M(R_{fin}),95high}}{R_{edge}}$$
(3.22)

Figure 3.9 shows how extending the radius changes the median escape velocities. As can be inferred, the density drops more quickly for LeoII than for Carina, since the escape velocity does not change as drastically when considering contributions from higher radii. This suggests higher accuracy of escape velocities calculated for LeoII.

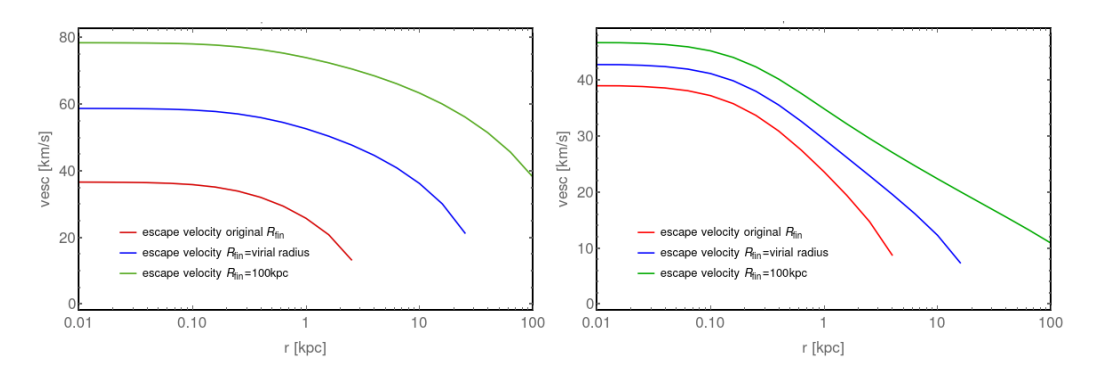


Figure 3.9: Escape velocities for Carina (left) and LeoII (right) for profiles extended to different radii: red for the original R_{edge} , blue for the Virial radius, and green for 100kpc

Using the coarse grained estimate for the lower mass bound described in section (1.1) and conservative error estimates, one derives:

$$m(r) = \left(\frac{h^3}{2} \frac{\rho(r)}{\frac{4}{3}\pi (v_{esc}^2)^{3/2}}\right)^{1/4}$$
(3.23)

$$\sigma_{m,low}(r) = m(r) - \left(\frac{h^3}{2} \frac{\rho(r) - \sigma_{\rho,low}(r)}{\frac{4}{3}\pi(v_{esc}^2(r) + \sigma_{v_{esc}^2,high}(r))^{3/2}}\right)^{1/4}$$
(3.24)

$$\sigma_{m,high}(r) = -m(r) + \left(\frac{h^3}{2} \frac{\rho(r) + \sigma_{\rho,high}}{\frac{4}{3}\pi (v_{esc}^2(r) - \sigma_{v_{esc}^2,low}(r))^{3/2}}\right)^{1/4}$$
(3.25)

which yields a lower bound at every radius (figure (3.10)) and appendix \mathbb{C}).

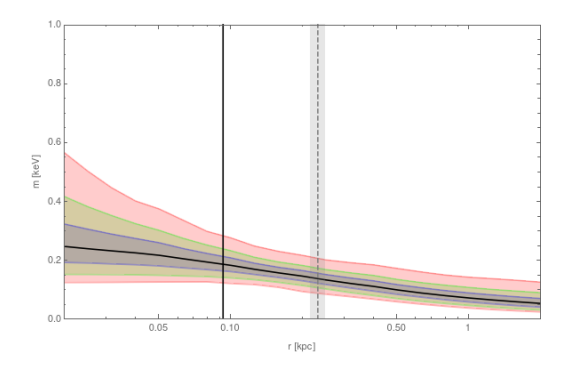


Figure 3.10: Lower mass bound for LeoII from data provided by Read et alii. The black line highlights the radius $0.4r_{12}$, the dashed line the half-light radius r_{12}

3.2 Mass bounds 53

	radius	mass bound from local ρ			
		R_{edge} = orig.	$R_{edge} = r_{vir}$	$R_{edge} = 100 \text{kpc}$	
Carina	at R_{start} at $0.4r_{12}$ at r_{12}	$\begin{array}{c} 0.231^{0.244}_{0.095} \\ 0.163^{0.051}_{0.034} \\ 0.126^{0.034}_{0.022} \end{array}$	$\begin{array}{c} 0.162^{0.251}_{0.074} \\ 0.112^{0.072}_{0.032} \\ 0.084^{0.052}_{0.022} \end{array}$	$\begin{array}{c} 0.130_{0.066}^{0.263} \\ 0.090_{0.036}^{0.086} \\ 0.067_{0.022}^{0.062} \end{array}$	
Draco	at R_{start} at $0.4r_{12}$ at r_{12}	$\begin{array}{c} 0.189^{0.117}_{0.051} \\ 0.150^{0.027}_{0.025} \\ 0.120^{0.016}_{0.015} \end{array}$	$\begin{array}{c} 0.160^{0.117}_{0.056} \\ 0.126^{0.033}_{0.033} \\ 0.099^{0.022}_{0.024} \end{array}$	$\begin{array}{c} 0.144_{0.063}^{0.120} \\ 0.113_{0.041}^{0.038} \\ 0.089_{0.030}^{0.027} \end{array}$	
LeoI	at R_{start} at $0.4r_{12}$ at r_{12}	$\begin{array}{c} 0.202^{0.256}_{0.084} \\ 0.138^{0.039}_{0.030} \\ 0.105^{0.026}_{0.019} \end{array}$	$\begin{array}{c} 0.183^{0.260}_{0.082} \\ 0.124^{0.046}_{0.033} \\ 0.093^{0.033}_{0.023} \end{array}$	$\begin{array}{c} 0.166_{0.084}^{0.269} \\ 0.112_{0.039}^{0.055} \\ 0.083_{0.027}^{0.040} \end{array}$	
LeoII	at R_{start} at $0.4r_{12}$ at r_{12}	$\begin{array}{c} 0.293^{0.261}_{0.118} \\ 0.202^{0.047}_{0.038} \\ 0.150^{0.031}_{0.025} \end{array}$	$\begin{array}{c} 0.273_{0.119}^{0.262} \\ 0.187_{0.045}^{0.053} \\ 0.138_{0.031}^{0.036} \end{array}$	$\begin{array}{c} 0.256_{0.127}^{0.267} \\ 0.174_{0.058}^{0.060} \\ 0.127_{0.041}^{0.041} \end{array}$	
Fornax	at R_{start} at $0.4r_{12}$ at r_{12}	$\begin{array}{c} 0.116^{0.098}_{0.037} \\ 0.084^{0.011}_{0.012} \\ 0.068^{0.007}_{0.008} \end{array}$	$\begin{array}{c} 0.102^{0.090}_{0.038} \\ 0.073^{0.011}_{0.016} \\ 0.058^{0.008}_{0.011} \end{array}$	$\begin{array}{c} 0.091_{0.041}^{0.084} \\ 0.065_{0.020}^{0.012} \\ 0.050_{0.015}^{0.009} \end{array}$	
Sextans	at R_{start} at $0.4r_{12}$ at r_{12}	$\begin{array}{c} 0.220^{0.264}_{0.094} \\ 0.118^{0.021}_{0.018} \\ 0.086^{0.024}_{0.021} \end{array}$	$\begin{array}{c} 0.193_{0.087}^{0.250} \\ 0.100_{0.022}^{0.025} \\ 0.068_{0.021}^{0.025} \end{array}$	$\begin{array}{c} 0.171_{0.086}^{0.245} \\ 0.087_{0.029}^{0.029} \\ 0.057_{0.022}^{0.028} \end{array}$	
Sculptor	at R_{start} at $0.4r_{12}$ at r_{12}	$ \begin{array}{c} 0.154^{0.110}_{0.040} \\ 0.125^{0.028}_{0.018} \\ 0.103^{0.016}_{0.011} \end{array} $	$\begin{array}{c} 0.116^{0.109}_{0.038} \\ 0.094^{0.036}_{0.021} \\ 0.075^{0.025}_{0.015} \end{array}$	$\begin{array}{c} 0.099_{0.038}^{0.112} \\ 0.080_{0.042}^{0.042} \\ 0.064_{0.017}^{0.029} \end{array}$	
UMi	at R_{start} at $0.4r_{12}$ at r_{12}	$ \begin{array}{c} 0.181^{0.147}_{0.053} \\ 0.127^{0.020}_{0.016} \\ 0.101^{0.014}_{0.014} \end{array} $	$\begin{array}{c} 0.144^{0.135}_{0.049} \\ 0.100^{0.025}_{0.020} \\ 0.076^{0.018}_{0.016} \end{array}$	$\begin{array}{c} 0.124_{0.049}^{0.133} \\ 0.085_{0.023}^{0.029} \\ 0.064_{0.018}^{0.021} \end{array}$	

Table 3.2: Mass bounds evaluated at three different radii (R_{start} near the center, $0.4r_{12}$, and r_{12}) for profiles extended to three different radii (original radius, Virial radius, 100kpc).

Table 3.2 displays mass bounds evaluated at different radii for each of the LG dSphs under consideration. The most relevant lower mass bound is that derived for LeoII. By increasing the considered range from around 15kpc to (the rather unphysical) 100 kpc, one lowers the derived value for LeoII by only 6%, lending further credibility to the robustness of the estimation.

3.2.3 Corrections

The previous dSph profiles derived by *Read et alii* model idealized versions of the galaxies (e.g. spherically symmetric, no tidal stripping by the host galaxy - see [33]). For this reason, we will attempt to remedy some of the dark matter mass

bound's inaccuracies with corrections based on simulations done by *Genina et alii* [33].

As a data set, *Genina et alii* choose the APOSTLE suite simulations of Milky Way and Andromeda analogue pairs (chosen to satisfy general constraints for the Local Group galaxies, such as total mass, separation and relative velocities) with population of dSphs. LG dSphs are considered to be in an instantaneous steady state. 25 dSphs are selected to match the properties of Milky Way dSphs (and specifically, Fornax) in terms of

- Stellar masses and number of stars
- Velocity dispersion
- Projected half light radii R_e
- Amount of bound gas (none)
- Amount of signs for rotation (little)
- Distance from host galaxy ($\leq 300kpc$)
- Sphericity s = c/a (ratio of minor to major axes), where Fornax corresponds to a s = 0.7, with an average of s = 0.9)

Positions and velocities of stars within dSphs are projected along one of either major, minor and intermediate axis to generate a photometric (random sample of 500 - 2500 stars within R_{2D}) and kinematic (all stars within R_{2D} perturbed with Gaussian noise) data for each star, which is split into bins and analysed using the process described in section (3.1.1).

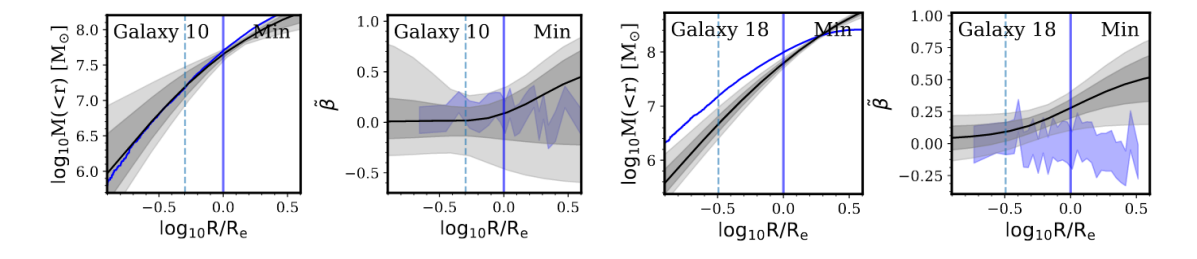


Figure 3.11: Results of the RS-model for two model dSphs. Black (grey) represents median (confidence intervals) for the recovered profiles, whereas blue stands for the "true" (i.e. simulated) profile. Taken from [33]

See figure (3.11) for examples of the reconstruction of simulated density profiles. For galaxy 10, viewed along the minor axis, enclosed mass and reduced velocity anisotropy β are well recovered. For galaxy 18, also viewed along the minor axis, a poor recovery of the velocity anisotropy (the method favours radial anisotropy) leads to an underestimation of the enclosed mass.

A few effects were found to reduce the accuracy of the model:

3.2 Mass bounds 55

• Line of sight effects.

For galaxies viewed along the minor or intermediate axis, enclosed masses are underestimated (with a factor down to 0.75); for the major axis they are slightly overestimated (up to 1.25) - see figure 3.12.

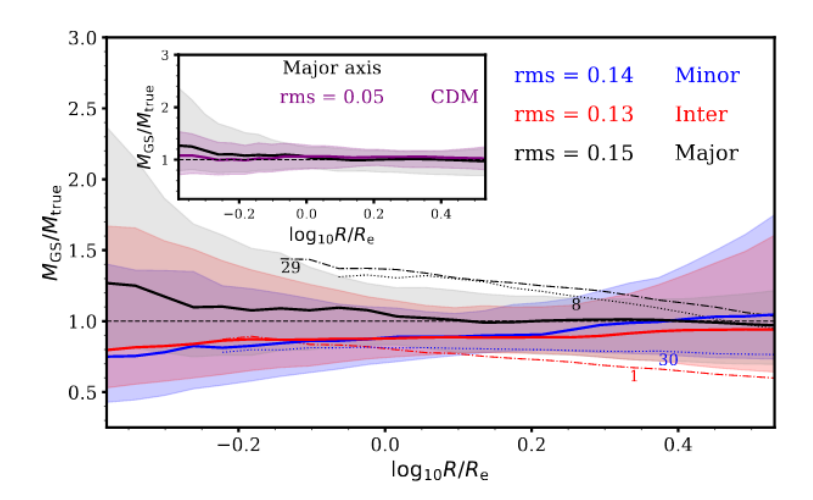


Figure 3.12: average ratio of reconstructed masses to true mass for galaxies projected along the minor (blue), intermediate (red), and major (black) axis. Taken from [33]

Aspherical dwarfs resemble the sample viewed along the major axis, since a majority of aspherical dwarfs were projected along the major axis. Excluding heavily aspherical dSphs from the sample of aspehrical dSphs increases accuracy and reduces scatter, suggesting accurate estimation for those dSph, which can be described as more spherical and which are projected along the major axis.

• Preference for radially biased anisotropy parameters
The RS model shows preference for radially biased velocity anisotropy when
the true profile is constant.

Poor velocity anisotropy recovery is related to inclusion of Virial shape parameters, as runs without VSPs show. The first Virial shape parameter (VSP1) strongly disfavours constant β (VSP2 is sensitive to noisy data in outer regions due to the R^3 term, permitting a wider range of profiles). Still, inclusion of VSP leads to better performance overall.

Tidal stripping

Satellites are subject to tidal stripping due to their host galaxies. From simulations *Genina et alii* infer that tidal stripping causes tangential anisotropies in outer regions of the galaxy (preferential stripping of radial orbits). LG dSphs with pericenters closer to the host galaxies lose more of their infall mass. Severley stripped dwarfs are those with distance below 40 kpc and more than 70% of stripped mass excluding highly aspherical dwarfs (i.e. asphericity effects), we see the effect of tidal stripping. In outer regions, mass

is overestimated. In the inner regions, tides tend to lead to an underestimation of the enclosed mass (factor of down to 0.8). For this, see figure (3.13). This is more significant if distance is lowered.

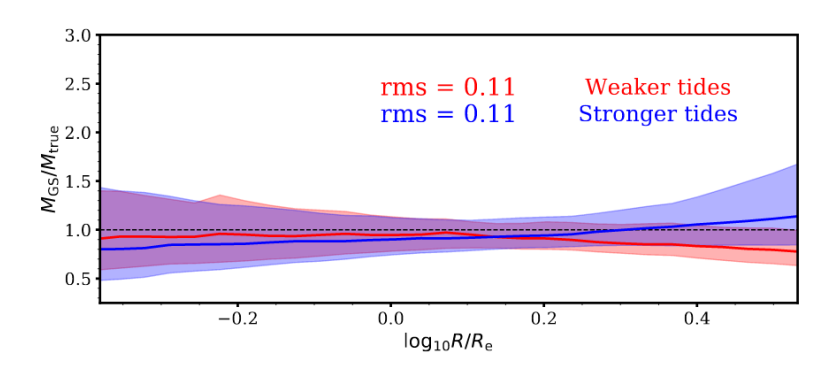


Figure 3.13: Effect of tides on estimation of enclosed mass profile

Consequences for our mass bound

As mentioned before, line of sight effects may lead to overestimation (factor of up to 1.25 across radial range for major axis projection of highly aspherical dwarfs) or underestimation (factor of down to 0.75 for intermediate or minor axis projection across radial range of mass profiles. Tidal stripping leads to an underestimation (factor down to 0.8 in inner regions) of mass profiles for galaxies <40kpc. For dark matter particle lower mass bounds I, therefore, propose a worst-case correction to enclosed masses of 0.8 for potentially tidally stripped dSphs $0.75 \cdot 0.8 = 0.6$ for aspheric, potentially tidally stripped dShs viewed along minor/intermediate axis 0.75 for aspherical dwarfs viewed along the minor/intermediate axis This will lead to m_{true} , a conservative correction in DM particle lower mass bound m:

Tidally stripped + inter./min. axis project:	inter./min. axis projection	Tidally stripped
$m \sim 0$	$\left(\frac{\rho}{v^3}\right)^{1/4} \sim \left(\frac{M}{M^{3/2}}\right)^{1/4} \sim M^{-1/8}$ $\mid M = 0.75 M_{true}$	
$M=0.6M_{true}$	$M = 0.75 M_{true}$	$M=0.8M_{true}$
	$rac{m}{m_{true}} \sim \left(rac{M}{M_{true}} ight)^{-1/8} \ \mid m_{true} = 0.964$	
$m_{true} = 0.938m$	$m_{true} = 0.964$	$m_{true} = 0.972$

Effects leading to overestimation are not considered here, since they only raise the lower mass bound (these effects would be small for less aspherical dwarfs. Severely tidally stripped dwarfs (i.e. correction of 0.94) are potentially those with distance to host galaxy of $\leq 40kpc$. All of the dSphs used for the DM particle lower mass bound are outside this radius (with UMi being the closest at 60kpc) -

3.2 Mass bounds 57

	m [keV]	m [keV]	m [keV]
	Read, Steger profile	Read, Steger profile	Boyarsky et alii
	extended	extended + LOS correction	[8]
Carina	$0.112_{0.032}^{0.072}$	$0.107_{0.031}^{0.069}$	$0.215_{0.032}^{0.050}$
Draco	$0.126_{0.033}^{0.033}$	$0.121_{0.032}^{0.023}$	$0.226_{0.016}^{0.020}$
Fornax	$0.102^{0.038}_{0.090}$	$0.098^{0.037}_{0.087}$	$0.164_{0.026}^{0.041}$
LeoI	$0.124_{0.033}^{0.046}$	$0.120^{0.044}_{0.032}$	$0.189_{0.034}^{0.059}$
LeoII	$0.187^{0.053}_{0.045}$	$0.180^{0.051}_{0.043}$	$0.269_{0.035}^{0.052}$
Sculptor	$0.116_{0.038}^{0.109}$	$0.112^{0.105}_{0.037}$	$0.264_{0.031}^{0.038}$
Sextans	$0.100^{0.025}_{0.022}$	$0.096^{0.024}_{0.021}$	$0.147^{0.044}_{0.026}$
UMi	$0.144_{0.049}^{0.135}$	$0.139^{0.130}_{0.047}$	$0.195^{0.051}_{0.031}$

Table 3.3: LOS corrected mass bounds for extended (up to Virial radius) profiles, evaluated at either R_{start} or $0.4r_{12}$, with data provided by Read et alii

see *Łokas et alii* [34]. We, therefore, apply the correction of $m_{true} = 0.964m$ to all of the dwarfs (see table 3.3).

Finally, we can pose:

$$m_{DM} \ge 180^{+51}_{-43} \,\text{eV}$$
 (3.26)

For a fermionic dark matter particle.

This is consistent with lower bounds derived with similar methods by other authors (e.g. 190 eV by Savchenko et Rudakovskyi [35] or 269 eV by Boyarsky et alii [8]).

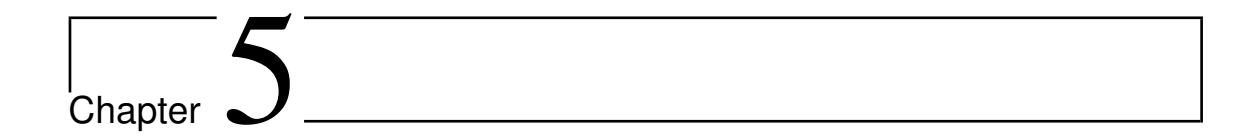


Acknowledgements

I would like to express my gratitude to Prof Alexey Boyarsky for supervising this project, for his suggestions and commentaries. Thanks also to Dr. Kyrylo Bondarenko, whose patient guidance, advice, and critiques of my work were greatly appreciated.

Much of this work would not have been possible without the density profile data provided by Dr Justin Read, for which I am very grateful.

Finally, I would like to thank my mother for her continued support and encouragement.



Bibliography

- [1] F. Zwicky, "Die rotverschiebung von extragalaktischen nebeln," *Helvetica Physica Acta, Vol. 6, p. 110-127,* 1933.
- [2] V. Trimble, "Existence and nature of dark matter in the universe," *Ann. Rev. Astron. Astrophys*, pp. 425–427, 1987.
- [3] S. M. Bucklin, "Arstechnica: A history of dark matter," *arstechnica.com/science/2017/02/a-history-of-dark-matter*, 2017.
- [4] G. Donatiello, "Sextans a dwarf spheroidal (sex a)," *flickr.com/photos/133259498@N05/44246501874*, 28. September 2018.
- [5] CERN-Physics, "Dark matter," home.cern/science/physics/dark-matter, 20 January 2012.
- [6] Caltech-Edu, "dwarf spheroidal galaxies," ned.ipac.caltech.edu/level5/March01/ Battaner/node13.html, Juni 2014.
- [7] S. Tremaine and J. E. Gunn, "Dynamical role of light neutral leptons in cosmology," *Physical Review Letters*, vol. 42, p. 407–410, May 1979.
- [8] A. Boyarsky, O. Ruchayskiy, and D. Iakubovskyi, "A lower bound on the mass of dark matter particles," *Journal of Cosmology and Astroparticle Physics*, vol. 2009, p. 005–005, Mar 2009.
- [9] E. L. Łokas, S. R. Majewski, S. Kazantzidis, L. Mayer, J. L. Carlin, D. L. Nidever, and L. A. Moustakas, "The shapes of milky way satellites: Looking for signatures of tidal stirring," *The Astrophysical Journal*, vol. 751, no. 1, p. 61, 2012.
- [10] J. Wolf, G. D. Martinez, J. S. Bullock, M. Kaplinghat, M. Geha, R. R. Munoz, J. D. Simon, and F. F. Avedo, "Accurate masses for dispersion-supported galaxies," *Monthly Notices of the Royal Astronomical Society*, 2010.

62 Bibliography

[11] S. Tremaine and J. Binney, *Galactic Dynamics*, ch. 4. Princeton University Press, 2 ed., 2008.

- [12] A. Evans, "Flickr: M31, the andromeda galaxy (now with h-alpha).," *flickr.com/photos/astroporn/4999978603/in/photostream/*, Sep 2010.
- [13] A. Burkert, "The structure and dark halo core properties of dwarf spheroidal galaxies," *arXiv*/1501.06604, 2015.
- [14] J. I. Read and P. Steger, "How to break the density-anisotropy degeneracy in spherical stellar systems," *Monthly Notices of the Royal Astronomical Society*, vol. 471, no. 4, p. 4541–4558, 2017.
- [15] T. Richardson and M. Fairbairn, "On the dark matter profile in sculptor: breaking the β degeneracy with virial shape parameters," *Monthly Notices of the Royal Astronomical Society*, vol. 441, p. 1584–1600, Dec 2014.
- [16] M. G. Walker, M. Mateo, E. W. Olszewski, J. Peñarrubia, N. W. Evans, and G. Gilmore, "A universal mass profile for dwarf spheroidal galaxies?," *The Astrophysical Journal*, vol. 704, p. 1274–1287, Jan 2009.
- [17] M. R. Merrifield and S. M. Kent, "Fourth moments and the dynamics of spherical systems," *The Astronomical Journal*, vol. 99, p. 1548, 1990.
- [18] L. Randall, J. Scholtz, and J. Unwin, "Cores in dwarf galaxies from fermi repulsion," *Monthly Notices of the Royal Astronomical Society*, 2017.
- [19] D. J. Griffiths, *Introduction to quantum mechanics*. *Second Edition*, ch. 5. Prentice Hall, 1995.
- [20] N. C. Amorisco, A. Agnello, and N. W. Evans, "The core size of the fornax dwarf spheroidal," *Monthly Notices of the Royal Astronomical Society: Letters*, vol. 429, no. 1, 2012.
- [21] T. Richardson and M. Fairbairn, "Cores in classical dwarf spheroidal galaxies? a dispersion-kurtosis jeans analysis without restricted anisotropy," 05 2013.
- [22] R. Ruffini, C. R. Arguelles, and J. A. Rueda, "On the core-halo distribution of dark matter in galaxies," *Monthly Notices of the Royal Astronomical Society*, vol. 451, no. 1, p. 622–628, 2015.
- [23] J. G. Gao, M. Merafina, and R. Ruffini, "The semidegenerate configurations of a selfgravitating system of fermions," *Astronomy and Astrophysics*, vol. 235, pp. 1–7, aug 1990.
- [24] O. Klein, "On the thermodynamical equilibrium of fluids in gravitational fields," *Reviews of Modern Physics*, vol. 21, p. 531–533, Jan 1949.

- [25] J. R. Oppenheimer and G. M. Volkoff, "On massive neutron cores," *Physical Review*, vol. 55, no. 4, p. 374–381, 1939.
- [26] D. S. Gorbunov and V. A. Rubakov, *Introduction to the Theory of the Early Universe; Thermodynamics in Expanding Universe*, p. 91–109. World Scientific Publishing, 2011.
- [27] W. J. G. D. Blok, F. Walter, E. Brinks, C. Trachternach, S.-H. Oh, and R. C. Kennicutt, "High-resolution rotation curves and galaxy mass models from things," *The Astronomical Journal*, vol. 136, no. 6, p. 2648–2719, 2008.
- [28] S. Brownsberger and L. Randall, "Stellar profile independent determination of the dark matter distribution of the fornax local group dwarf spheroidal galaxy," arXiv/1912.01634, 2019.
- [29] A. C. Robin, C. Reylé, J. Fliri, M. Czekaj, C. P. Robert, and A. M. M. Martins, "Constraining the thick disc formation scenario of the milky way," *Astronomy & Astrophysics*, vol. 569, 2014.
- [30] T. The-Hubble-Heritage-Team (AURA/STScI/NASA), "Ngc 4414," en.wikipedia.org/wiki/File:NGC_4414_(NASA-med).jpg, 3 June 1999.
- [31] M. Walker and J. Penarrubia, "Spherical models for the gaia challenge," *data:gaiachallenge_spherical.pdf*, 2013.
- [32] M. G. Walker, M. Mateo, and E. W. Olszewski, "Stellar velocities in the carina, fornax, sculptor, and sextans dsph galaxies: Data from the magellan/mmfs survey," *The Astronomical Journal*, vol. 137, pp. 3100–3108, Feb. 2009.
- [33] A. Genina, J. I. Read, C. S. Frenk, S. Cole, A. Benitez-Llambay, A. D. Ludlow, J. F. Navarro, K. A. Oman, and A. Robertson, "To beta or not to beta: can higher-order jeans analysis break the mass-anisotropy degeneracy in simulated dwarfs?," 2019.
- [34] E. Łokas, S. Majewski, S. Kazantzidis, L. Mayer, J. Carlin, D. Nidever, and L. Moustakas, "The shapes of milky way satellites: Looking for signatures of tidal stirring," *Astrophysical Journal*, vol. 751, 12 2011.
- [35] D. O. Savchenko and A. Rudakovskyi, "New mass bound on fermionic dark matter from a combined analysis of classical dsphs," *Monthly Notices of the Royal Astronomical Society*, vol. 487, pp. 5711–5720, 2019.
- [36] K. Bondarenko, A. Boyarsky, T. Bringmann, and A. Sokolenko, "Constraining self-interacting dark matter with scaling laws of observed halo surface densities," *Journal of Cosmology and Astroparticle Physics*, vol. 2018, no. 04, p. 049–049, 2018.



Deriving Jeans and Virial equations

A.1 Deriving the 2nd order Jeans equation

The following is a derivation of the 2nd order Jeans-equation, which (similarly to the derivation of Boltzmann equations, velocity moments, and all other Jeans equations) closely follows *Binney et Tremaine* [11]. The 2nd order Jeans equation in spherical coordinates is obtained by integrating the spherical Boltzmann equation (see equation (1.14)) over d^3p :

$$\frac{\partial}{\partial t} \int f p_r d^3 p + \frac{\partial}{\partial r} \int p_r^2 f d^3 p + \frac{1}{r^2} \frac{\partial}{\partial \theta} \int p_{\theta} f p_r d^3 p
+ \frac{1}{r^2 \sin^2 \theta} \frac{\partial}{\partial \phi} \int f p_{\phi} p_r d^3 p - \int (\frac{\partial \Phi}{\partial r} - \frac{p_{\theta}^2}{r^3} - \frac{p_{\phi}^2}{r^3 \sin^2 \theta}) \frac{\partial f}{\partial p_r} p_r d^3 p
- \int (\frac{\partial \Phi}{\partial \theta} - \frac{p_{\phi}^2 \cos \theta}{r^2 \sin^3 \theta}) \frac{\partial f}{\partial p_{\theta}} p_r d^3 p - \int \frac{\partial \Phi}{\partial \phi} \frac{\partial f}{\partial p_{\phi}} p_r d^3 p = 0$$
(A.1)

The last two integrals in equation (A.1) evaluate to zero, as they can be rewritten purely in terms of surface integrals. Using equations (1.19):

$$\frac{\partial}{\partial t}\rho r^{2}\sin\theta\overline{p_{r}} + \frac{\partial}{\partial r}\overline{p_{r}^{2}}\rho r^{2}\sin\theta + \frac{\partial}{\partial \theta}\sin\theta\rho\overline{p_{\theta}p_{r}} + \frac{1}{\sin\theta}\frac{\partial}{\partial \theta}\rho\overline{p_{\phi}p_{r}} - \int (\frac{\partial\Phi}{\partial r} - \frac{p_{\theta}^{2}}{r^{3}} - \frac{p_{\phi}^{2}}{r^{3}\sin^{2}\theta})fd^{3}p = 0$$

further simplified:

$$\frac{\partial}{\partial t}\rho r^{2}\sin\theta\overline{p_{r}} + \frac{\partial}{\partial r}\overline{p_{r}^{2}}\rho r^{2}\sin\theta + \frac{\partial}{\partial \theta}\sin\theta\rho\overline{p_{\theta}}\overline{p_{r}} + \frac{1}{\sin\theta}\frac{\partial}{\partial \phi}\rho\overline{p_{\phi}}\overline{p_{r}}$$
$$+r^{2}\sin\theta\rho\frac{\partial\Phi}{\partial r} - \frac{\sin\theta}{r}\overline{p_{\theta}^{2}}\rho - \frac{\overline{p_{\phi}^{2}}}{r\sin\theta}\rho = 0$$

noting that moments of uneven p_r (e.g. $\overline{p_r}$, $\overline{p_r}p_{\theta}$) vanish due to the density function being an even function of p_r ; rewriting momentum coordinates with velocity

coordinates; and dividing by $\sin \theta$, we arrive at:

$$\begin{split} \overline{v_r^2}\rho 2r + r^2 \frac{\partial}{\partial r} \overline{v_r^2}\rho + r^2 \rho \frac{\partial \Phi}{\partial r} - r \overline{v_\theta^2}\rho - r \overline{v_\phi^2}\rho &= 0 \\ \frac{\partial}{\partial r} \overline{v_r^2}\rho + \rho \frac{\partial \Phi}{\partial r} + \frac{1}{r} \rho \overline{v_r^2} 2 (-\frac{\overline{v_\theta^2} + \overline{v_\phi^2}}{2\overline{v_r^2}} + 1) &= 0 \end{split}$$

A.2 Deriving the Virial equation

We, now, set out to prove equation (1.34).

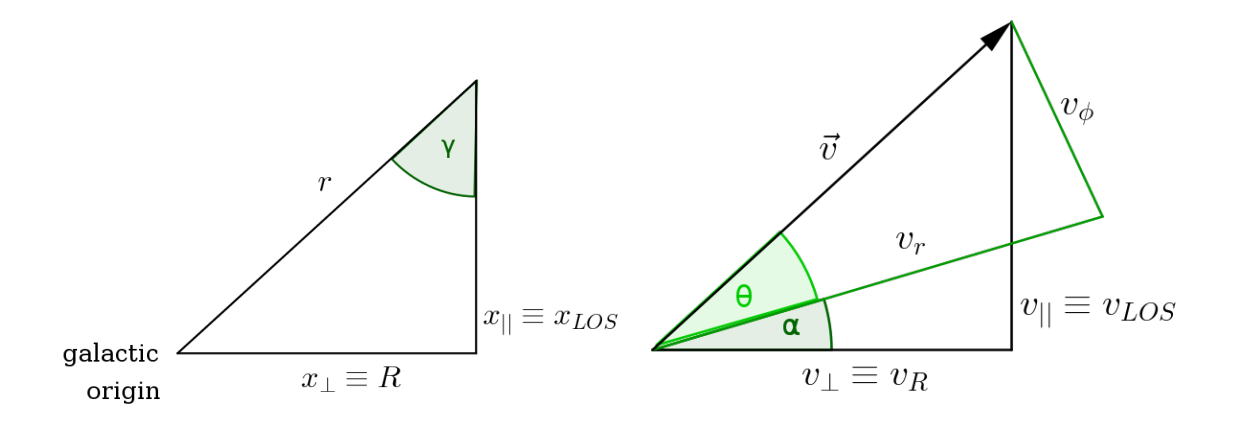


Figure A.1: Relationships between angles for (left) positions and (right) stellar velocities (viewed along the z-axis).

Proof. As previously shown and based on [11], the line of sight velocity dispersion can be expressed as

$$v_{||}^{2}(x_{\perp}) = \frac{\int \int dx_{||} d^{3}v \cdot v_{||}^{2}(\mathbf{x})\rho(\mathbf{x})P_{\mathbf{x}}(\mathbf{v})}{\int \rho(\mathbf{x})dx_{||}}$$

$$= \frac{\int dx_{||} \overline{v_{||}^{2}}\rho(\mathbf{x})}{\Sigma(x_{\perp})}$$
(A.2)

Note that $R \equiv x_{\perp}$, as well as $v_{LOS} \equiv v_{||}$, and $x_{LOS} \equiv x_{||}$ (see figure (A.1)). With this justification, these variables will be used interchangeably. Using a coordinate transformation from coordinate r to $x_{||}$ (via $r^2 = x_{||}^2 + x_{\perp}^2$) and the relations seen

in figure (A.1), one may rewrite the right-hand side of equation 1.34 as

$$2\int_{R}^{\infty} \left(1 - \beta(r) \frac{R^{2}}{r^{2}}\right) \frac{\rho(r) \overline{v_{r}^{2}(r)} r}{\sqrt{r^{2} - R^{2}}} dr = 2\int_{-\infty}^{\infty} \left(1 - \beta \frac{R^{2}}{r^{2}}\right) \rho \overline{v_{r}^{2}} dx_{||}$$

$$= 2\int_{-\infty}^{\infty} \left(\overline{v_{r}^{2}} - (\overline{v_{r}^{2}} - \frac{\overline{v_{t}^{2}}}{2}) \frac{R^{2}}{r^{2}}\right) \rho dx_{||}$$

$$= 2\int_{-\infty}^{\infty} \frac{\overline{v_{r}^{2}} x_{||}^{2} + \frac{1}{2} \overline{v_{t}^{2}} x_{\perp}^{2}}{x_{||}^{2} + x_{\perp}^{2}} \rho dx_{||}$$

$$= 2\int_{-\infty}^{\infty} (\overline{v_{r}^{2}} \cos^{2} \gamma + \overline{v_{\phi}^{2}} \sin^{2} \gamma) \rho dx_{||}$$

$$= 2\int_{-\infty}^{\infty} \overline{(v_{r} \cos \gamma + v_{\phi} \sin \gamma)^{2}} \rho dx_{||}$$

$$= 2\int_{-\infty}^{\infty} \overline{(v_{r} \sin \alpha + v_{\phi} \cos \alpha)^{2}} \rho dx_{||}$$

$$= \int \overline{v_{||}^{2}} \rho dx_{||}$$

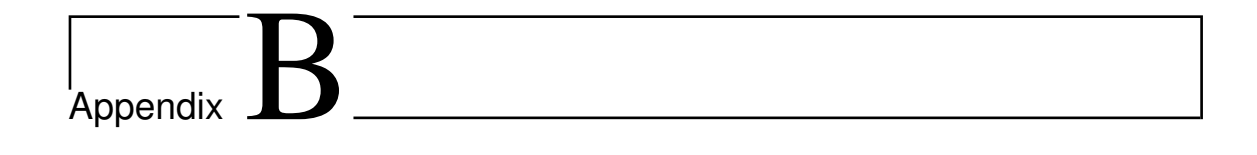
$$= \Sigma(R) v_{LOS}^{2}(R)$$

Where α is the angle between v_r and v_{\perp} , and γ the angle between the radial and the line-of-sight coordinate. Note that $\overline{v_r v_{\phi}} = 0$. From figure (A.1), we infer:

$$v_{||} = |\vec{v}|\sin(\theta + \alpha) = |\vec{v}|(\cos\theta\sin\alpha + \sin\theta\cos\alpha) = v_r\sin\alpha + v_\phi\cos\alpha \quad (A.4)$$

$$\cos(\alpha) = \cos(\pi/2 - \gamma) = \sin(\gamma) \tag{A.5}$$

$$\sin(\alpha) = \sin(\pi/2 - \gamma) = \cos(\gamma) \tag{A.6}$$



Density profiles

B.1 Density profile comparison

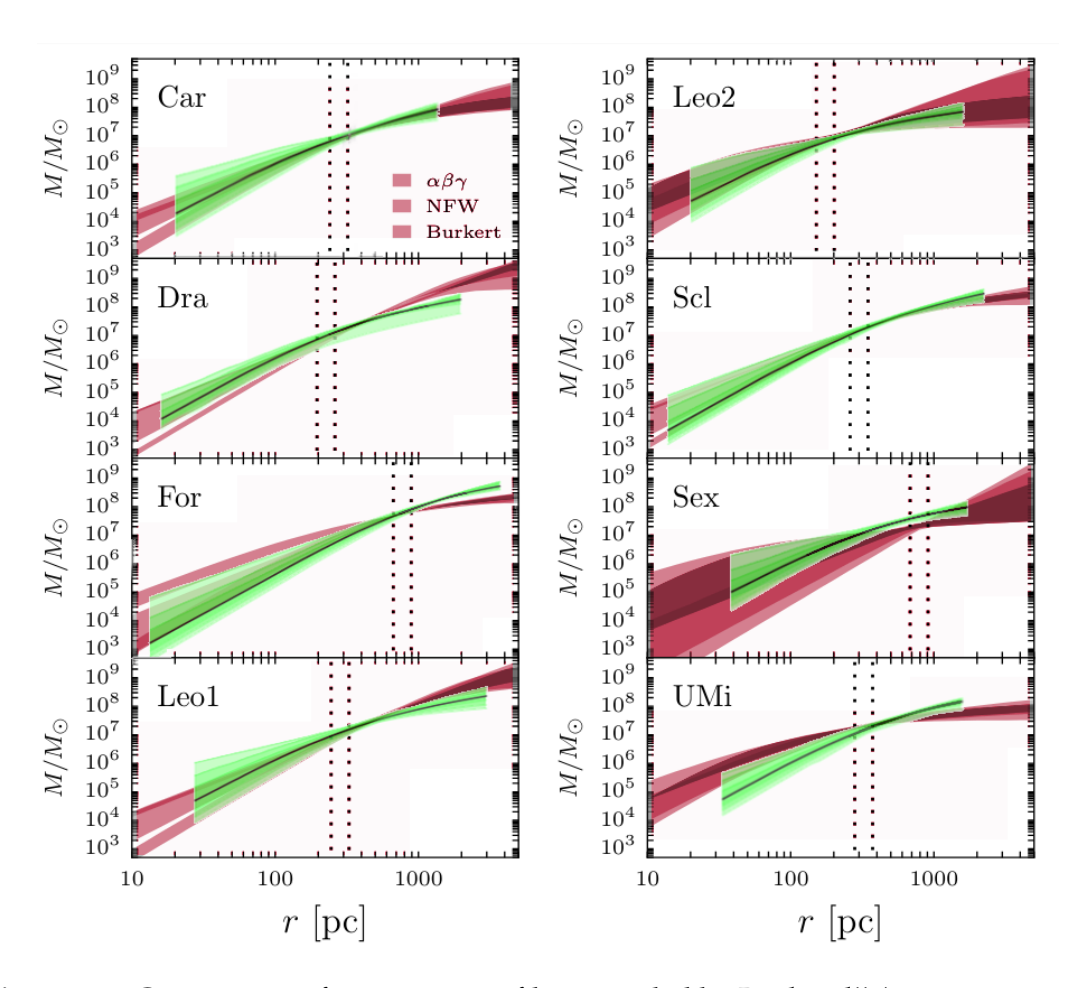


Figure B.1: Comparison of new mass profiles provided by Read et alii (green curves with 99% confidence interval) to those taken from Bondarenko et alii [36] (red curves with the same confidence interval for several parametrizations)



Mass Bounds

Black lines refer to a radius of $0.4r_{12}$ and dashed lines to the half-light radius r_{12} .

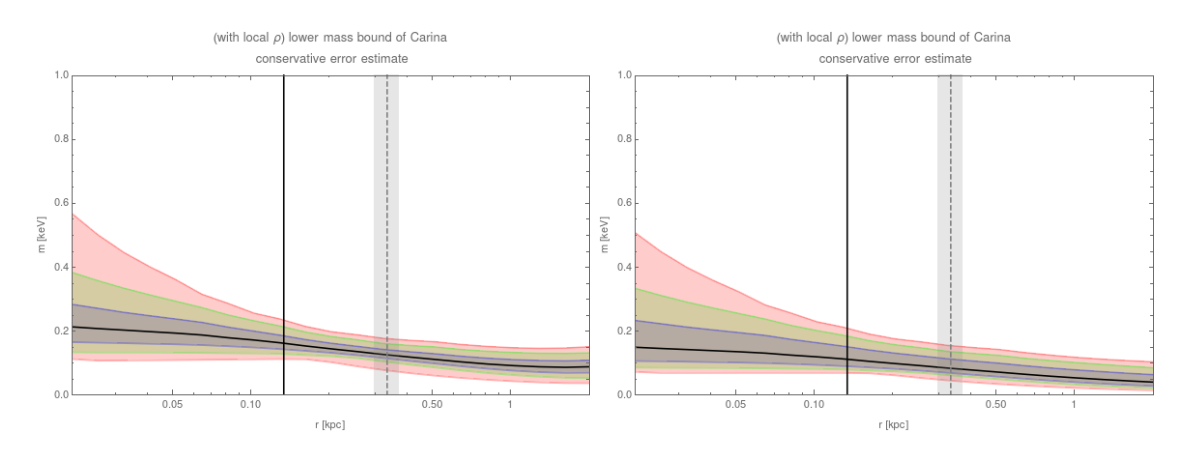


Figure C.1: Carina, mass bounds for a profile extended to a) ca 1.5kpc, b) Virial radius (ca 15kpc).

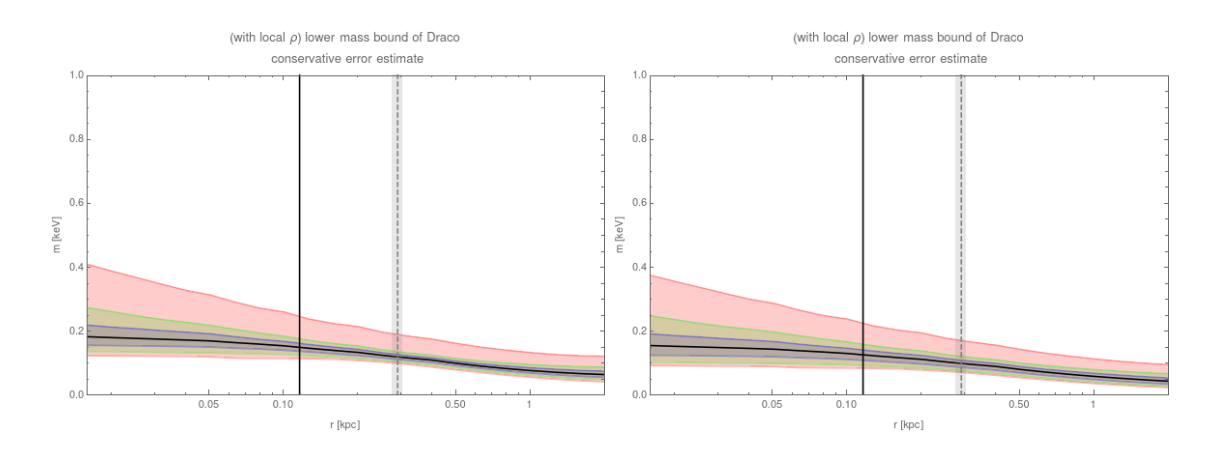


Figure C.2: Draco, mass bounds for a profile extended to a) ca 1.5kpc, b) Virial radius (ca 15kpc)

72 Mass Bounds

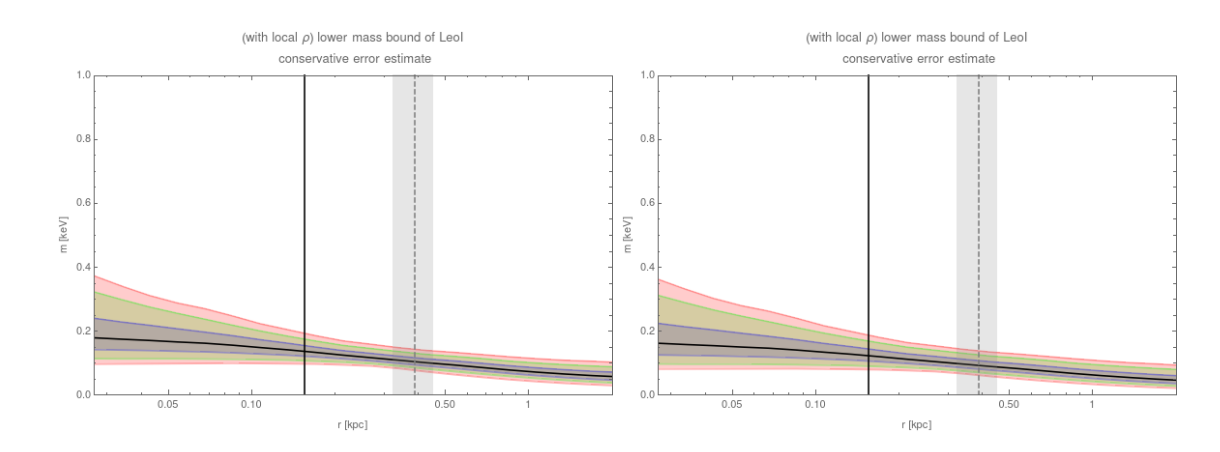


Figure C.3: LeoI, mass bounds for a profile extended to a) ca 1.5kpc, b) Virial radius (ca 15kpc)

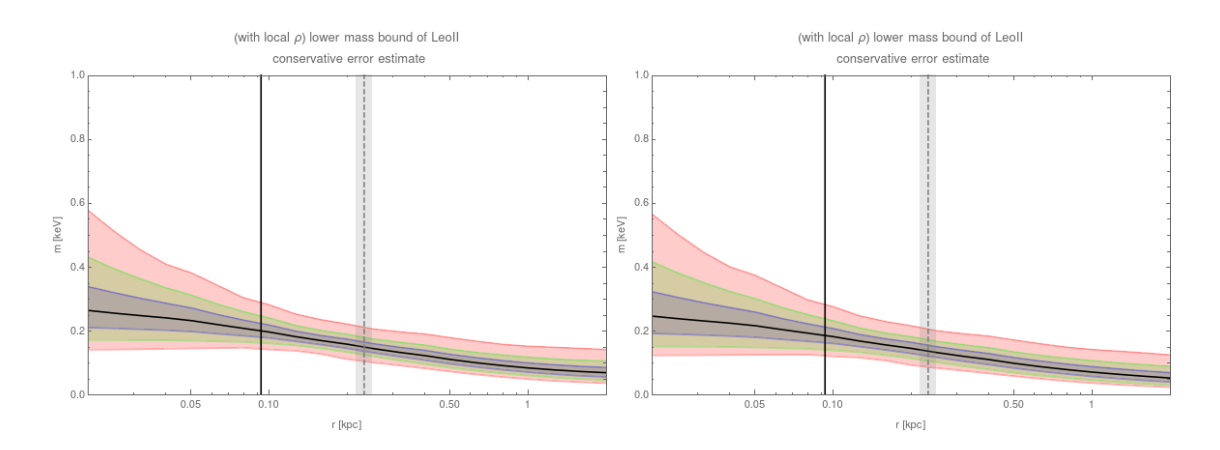


Figure C.4: LeoII, mass bounds for a profile extended to a) ca 1.5kpc, b) Virial radius (ca 15kpc)

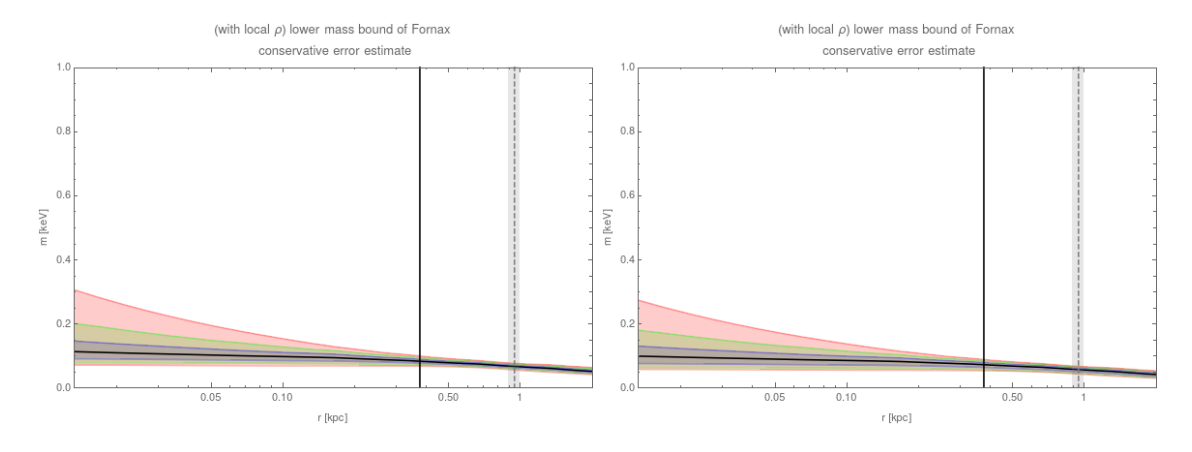


Figure C.5: Fornax, mass bounds for a profile extended to a) ca 1.5kpc, b) Virial radius (ca 15kpc)

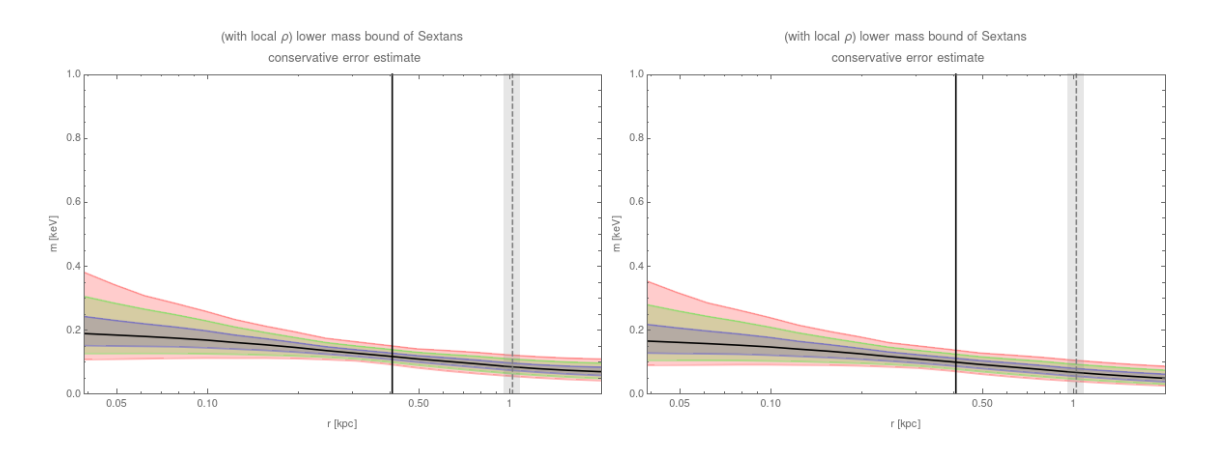


Figure C.6: Sextans, mass bounds for a profile extended to a) ca 1.5kpc, b) Virial radius (ca 15kpc)

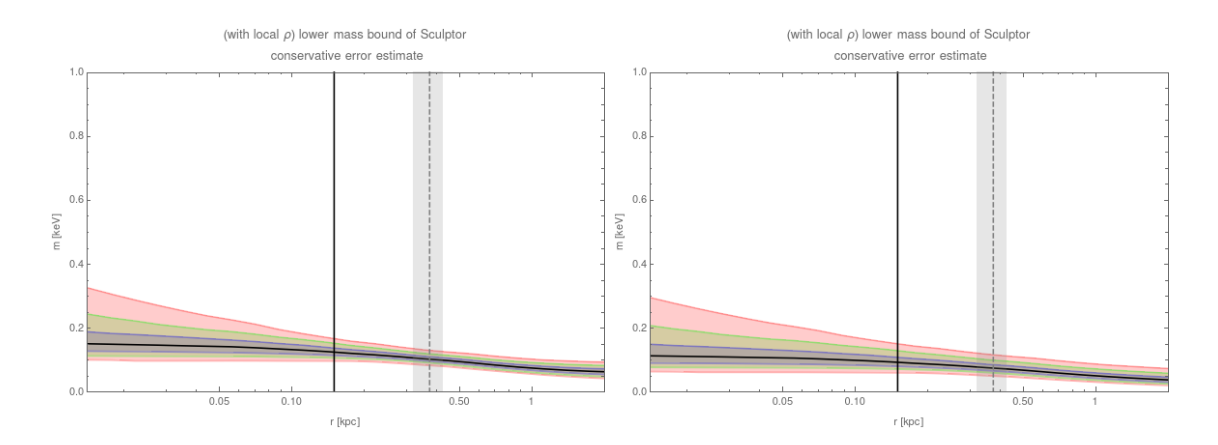


Figure C.7: Scuptor, mass bounds for a profile extended to a) ca 1.5kpc, b) Virial radius (ca 15kpc)

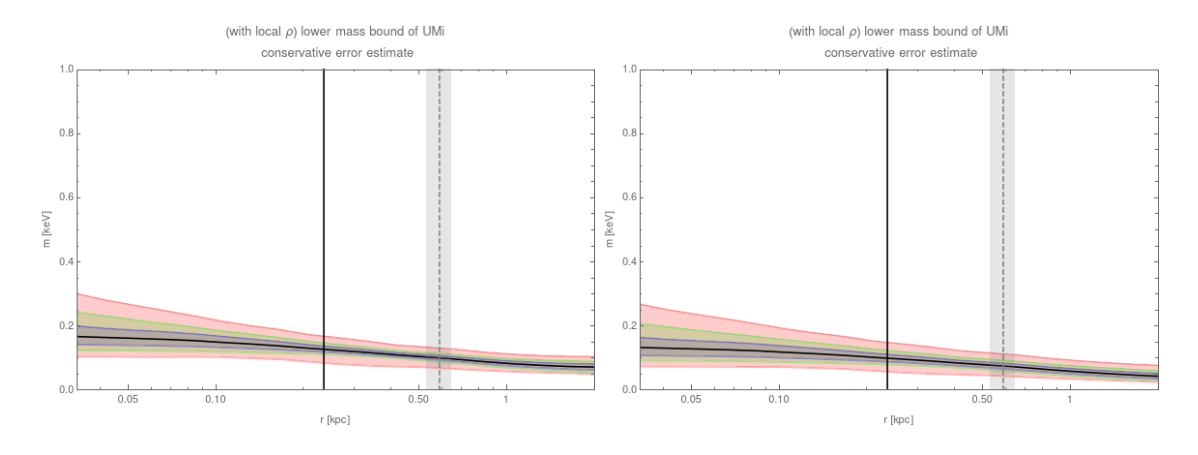


Figure C.8: UMi, mass bounds for a profile extended to a) ca 1.5kpc, b) Virial radius (ca 15kpc)